



Queensland University of Technology
Brisbane Australia

This is the author's version of a work that was submitted/accepted for publication in the following source:

Blackburn, Octavia A., Coe, Benjamin J., Hahn, Valentine, Helliwell, Madeleine, Raftery, James, Ta, Yien T., Peter, Laurence M., Wang, Hongxia, Anta, Juan A., & Guillén, Elena (2012) N-Aryl stilbazolium dyes as sensitizers for solar cells. *Dyes and Pigments*, 92(1), pp. 766-777.

This file was downloaded from: <http://eprints.qut.edu.au/46442/>

© Copyright 2011 Elsevier Ltd. All rights reserved. — This is the author's version of a work that was accepted for publication in *Dyes and Pigments*. Changes resulting from the publishing process, such as peer review, editing, corrections, structural formatting, and other quality control mechanisms may not be reflected in this document. Changes may have been made to this work since it was submitted for publication. A definitive version was subsequently published in *Dyes and Pigments*, [92, 1, (2011)] DOI: 10.1016/j.dyepig.2011.06.017

Notice: *Changes introduced as a result of publishing processes such as copy-editing and formatting may not be reflected in this document. For a definitive version of this work, please refer to the published source:*

<http://dx.doi.org/10.1016/j.dyepig.2011.06.017>

N-Aryl Stilbazolium Dyes as Sensitizers for Solar Cells

Octavia A. Blackburn^a, Benjamin J. Coe^{a,*}, Valentine Hahn^a, Madeleine Helliwell^a, James Raftery^a, Yien T. Ta^a, Laurence M. Peter^b, Hongxia Wang,^b Juan A. Anta,^c Elena Guillén^c

^a *School of Chemistry, University of Manchester, Oxford Road, Manchester M13 9PL, UK*

^b *Department of Chemistry, University of Bath, Bath BA2 5NB, UK*

^c *Area de Química Física, Departamento de Sistemas Físicos, Químicos y Naturales, Universidad Pablo de Olavide, 41013 Sevilla, Spain*

* Corresponding author. Tel.: +44 161 275 4601; fax: +44 161 275 4598.

E-mail address: b.coe@manchester.ac.uk (B.J. Coe).

1. Introduction

Given the urgent need to develop clean and renewable energy sources, there is much current interest in using molecular dyes, especially transition metal complexes, as sensitizers in solar energy harvesting [1]. Traditional solar cells rely on the direct absorption of photons by a semiconductor, but their efficiency is limited because visible light absorption requires narrow band-gap semiconductors which are inherently unstable with respect to photodegradation. In a major breakthrough in 1991, O'Regan and Grätzel reported efficient photosensitization of a wide band-gap semiconductor by a trinuclear Ru^{II}-2,2'-bipyridyl-based dye [2]. The chromophoric properties of such complexes derive from intense, low energy metal-to-ligand charge-transfer transitions.

A dye-sensitized solar cell (DSSC) contains a nanoparticulate film of a wide band-gap semiconductor such as TiO₂, coated with a dye monolayer. Photoexcitation of the dye results in electron injection into the conduction band of the semiconductor, and the dye is then regenerated by a species in the electrolyte (usually an organic solvent containing the I⁻/I₃⁻ couple). Driven largely by the desire to avoid the use of relatively expensive metals such as ruthenium, many recent studies have focused on using purely organic dyes in DSSCs [3]. Although such an approach initially proved somewhat less effective when compared with using metal-based dyes, state-of-the-art organic sensitizers are now becoming competitive [4].

Motivated by potential applications in the field of nonlinear optics, we have investigated previously a range of stilbazolium dyes that contain *N*-arylpyridinium groups which act as strong electron acceptors [5]. Although pyridinium groups are often exploited in nonlinear optical chromophores [6], and also as electron acceptors in other photo-active molecular assemblies [7], we are not aware of any instances in which such substituents have been used in dyes for solar cell applications. Since they are much stronger electron acceptors than a carboxylate group which is typically found in dye sensitizers, strongly red-shifted intramolecular charge-transfer (ICT)

bands may be anticipated; increased absorption into the red and NIR regions will improve matching with the AM 1.5 solar spectrum when compared with most existing sensitizers. In addition, the ICT absorptions of previously studied *N*-arylstilbazolium species are relatively intense (with molar extinction coefficients ϵ of up to ca. 75,000 $\text{M}^{-1} \text{cm}^{-1}$), fulfilling another of the key requirements for potentially efficient sensitization. This report concerns experimental and theoretical studies with two such new chromophores functionalized with ester groups which act as precursors to carboxylate units for anchoring to oxide surfaces.

2. Experimental

2.1. Materials and procedures

We have reported previously the synthesis of the precursor compound *N*-(2,4-dinitrophenyl)-4-picolinium chloride, [dnppic⁺]Cl; this material is unstable in air and quickly forms a tar-like substance which may be converted into its PF₆⁻ salt for improved handling [5a]. Therefore, [dnppic⁺]Cl was treated as a reactive intermediate in this study and used without purification for reactions with aniline derivatives. All other reagents were obtained commercially and used as supplied. Products were dried at room temperature in a vacuum desiccator (CaSO₄).

2.2. General physical measurements

¹H NMR spectra were recorded on a Bruker AV-400 spectrometer and all shifts are referenced to TMS. The fine splitting of pyridyl or phenyl ring AA'BB' patterns is ignored and the signals are reported as simple doublets, with *J* values referring to the two most intense peaks. Elemental analyses were performed by the Microanalytical Laboratory, University of Manchester. IR spectroscopy was performed on solid samples using an Excalibur BioRad FT-IR spectrometer, and UV-vis spectra were obtained by using a Shimadzu UV-2401 PC spectrophotometer. Mass spectra were measured by using +electrospray on a Micromass Platform II spectrometer with acetonitrile as the solvent.

Cyclic voltammetric measurements were carried out with an Ivium CompactStat. An EG&G PAR K0264 single-compartment microcell was used with a silver/silver chloride reference electrode (3 M NaCl, saturated AgCl) separated by a salt bridge from a glassy carbon disk working electrode and Pt wire auxiliary electrode. Acetonitrile was freshly distilled (from CaH₂) and [N(C₄H₉-*n*)₄]PF₆, as supplied from Fluka, was used as the supporting electrolyte. Solutions containing ca.

10^{-3} M analyte (0.1 M electrolyte) were deaerated by purging with N_2 . All $E_{1/2}$ values were calculated from $(E_{pa} + E_{pc})/2$ at a scan rate of 200 mV s^{-1} .

2.3. Synthesis

2.3.1. *N*-(3,5-Bismethoxycarbonylphenyl)-4-picolinium chloride, [(3,5-*MC*₂Ph)pic⁺]Cl

A solution of 4-picoline (2.4 mL, 25 mmol) and 2,4-dinitrochlorobenzene (5.00 g, 25 mmol) in ethanol (25 mL) was heated under reflux for 2 h. After cooling to room temperature, diethyl ether was added and the black precipitate was filtered off, washed with diethyl ether and dried. The crude product was purified by precipitation from boiling ethanol/diethyl ether. The resulting gray solid was filtered off, washed with diethyl ether and dried to afford crude [dnppic⁺]Cl (5.01 g). A portion of this material, assumed to be monohydrated (0.500 g, 1.59 mmol), and dimethoxy-5-aminoisophthalate (3.54 g, 16.9 mmol) were added to isopropanol (50 mL), and the suspension was heated at reflux for 72 h. After cooling to room temperature, a dark green/brown residue was filtered off. The yellow filtrate was evaporated to dryness, then dissolved in water (100 mL) and extracted with chloroform. The pale brown aqueous layer was reduced to dryness giving the crude product (0.305 g). Purification was effected by column chromatography on silica gel eluting with 80:20 dichloromethane/methanol. The major colourless band (fluorescent under short-wave UV light) was collected and evaporated to dryness to afford a peach-coloured solid. Yield: 0.194 g (35%, based on [dnppic⁺]Cl•H₂O; 23% based on 4-picoline). δ_H (400 MHz, CD₃OD) 9.15 (2 H, d, $J = 6.8$ Hz, C₅H₄N), 8.87 (1 H, t, $J = 1.5$ Hz, C₆H₃), 8.67 (2 H, d, $J = 1.5$ Hz, C₆H₃), 8.17 (2 H, d, $J = 6.3$ Hz, C₅H₄N), 4.02 (6 H, s, 2CO₂Me), 2.83 (3 H, s, Me). $\nu(C=O)$ 1734s cm^{-1} . Anal. Calcd (%) for C₁₆H₁₆ClNO₄•1.3H₂O: C, 55.67; H, 5.43; N, 4.06. Found: C, 55.56; H, 5.10; N, 3.88. m/z : 286 ([M - Cl]⁺).

2.3.2. *N*-(4-Methoxycarbonylphenyl)-4-picolinium chloride, [(4-MCPh)pic⁺]Cl

This compound was prepared and purified in a manner similar to [(3,5-MC₂Ph)pic⁺]Cl•1.25H₂O by using methyl-4-aminobenzoate (2.56 g, 16.9 mmol) in place of dimethoxy-5-aminoisophthalate (crude product = 0.246 g). The product was finally crystallized by diffusion of diethyl ether vapour into an ethanol solution. Yield: 63 mg (14%, based on [dnppic⁺]Cl•H₂O; 9% based on 4-picoline). δ_{H} (400 MHz, CD₃OD) 9.13 (2 H, d, J = 6.8 Hz, C₅H₄N), 8.35 (2 H, d, J = 8.8 Hz, C₆H₄), 8.15 (2 H, d, J = 6.3 Hz, C₅H₄N), 7.97 (2 H, d, J = 9.1 Hz, C₆H₄), 3.99 (3 H, s, CO₂Me), 2.81 (3 H, s, Me). $\nu(\text{C=O})$ 1717 s cm⁻¹. Anal. Calcd (%) for C₁₄H₁₄ClNO₂•0.8H₂O: C, 60.46; H, 5.65; N, 5.04. Found: C, 60.31; H, 5.56; N, 5.12. m/z : 228 ([M - Cl]⁺).

2.3.3. (*E*)-4'-(Dimethylamino)-*N*-(3,5-bismethoxycarbonylphenyl)-4-stilbazolium hexafluorophosphate, [1]PF₆

[(3,5-MC₂Ph)pic⁺]Cl•1.3H₂O (100 mg, 0.290 mmol), 4-(dimethylamino)benzaldehyde (102 mg, 0.684 mmol) and piperidine (4 drops) were added to methanol (20 mL) and the mixture was heated at reflux for 4 h. Addition of diethyl ether (200 mL) to the purple solution afforded a dark precipitate which was filtered off, washed with diethyl ether and dried. Data for crude chloride salt, [1]Cl: δ_{H} (400 MHz, CD₃OD) 8.86–8.84 (3 H, C₅H₄N + C₆H₃), 8.61 (2 H, d, J = 1.5 Hz, C₆H₃), 8.12 (2 H, d, J = 7.1 Hz, C₅H₄N), 8.02 (1 H, d, J = 15.6 Hz, CH), 7.68 (2 H, d, J = 9.1 Hz, C₆H₄), 7.20 (1 H, d, J = 15.9 Hz, CH), 6.81 (2 H, d, J = 9.1 Hz, C₆H₄), 4.02 (6 H, s, 2CO₂Me), 3.10 (6 H, s, NMe₂). $\nu(\text{C=O})$ 1721 s cm⁻¹. This material was dissolved in 1:1 water/methanol and aqueous NH₄PF₆ (1 M) was added to give a dark purple precipitate which was filtered off, washed with water and dried. Yield: 120 mg (72%). δ_{H} (400 MHz, CD₃COCD₃) 9.12 (2 H, d, J = 7.1 Hz, C₅H₄N), 8.79 (1 H, t, J = 1.4 Hz, C₆H₃), 8.70 (2 H, d, J = 1.5 Hz, C₆H₃), 8.31 (2 H, d, J = 7.1 Hz, C₅H₄N), 8.17 (1 H, d, J = 15.9 Hz, CH), 7.71 (2 H, d, J = 9.1 Hz, C₆H₄), 7.36 (1 H, d, J = 16.1 Hz, CH), 6.85 (2 H, d, J = 9.1 Hz, C₆H₄), 4.00 (6 H, s, 2CO₂Me), 3.12 (6 H, s, NMe₂).

$\nu(\text{C}=\text{O})$ 1726s cm^{-1} . Anal. Calcd (%) for $\text{C}_{25}\text{H}_{25}\text{F}_6\text{N}_2\text{O}_4\text{P}\cdot 0.5\text{H}_2\text{O}$: C, 52.54; H, 4.59; N, 4.90. Found: C, 52.40; H, 4.48; N, 4.68. m/z : 417 ($[\text{M} - \text{PF}_6]^+$).

2.3.4. *(E)-4'-(Diphenylamino)-N-(3,5-bismethoxycarbonylphenyl)-4-stilbazolium hexafluorophosphate, [2]PF₆*

This compound was prepared in a manner similar to [1]PF₆ by using 4-(diphenylamino)benzaldehyde (187 mg, 0.684 mmol) in place of 4-(dimethylamino)benzaldehyde to give a dark red solid. Yield: 177 mg (88%). δ_{H} (400 MHz, CD_3COCD_3) 9.25 (2 H, d, $J = 7.1$ Hz, $\text{C}_5\text{H}_4\text{N}$), 8.81 (1 H, t, $J = 1.5$ Hz, C_6H_3), 8.73 (2 H, d, $J = 1.5$ Hz, C_6H_3), 8.45 (2 H, d, $J = 7.1$ Hz, $\text{C}_5\text{H}_4\text{N}$), 8.21 (1 H, d, $J = 16.1$ Hz, CH), 7.72 (2 H, d, $J = 8.8$ Hz, C_6H_4), 7.53 (1 H, d, $J = 16.1$ Hz, CH), 7.43–7.39 (4 H, Ph), 7.24–7.18 (6 H, Ph), 7.01 (2 H, d, $J = 8.8$ Hz, C_6H_4), 4.01 (6 H, s, 2CO₂Me). $\nu(\text{C}=\text{O})$ 1730s cm^{-1} . Anal. Calcd (%) for $\text{C}_{35}\text{H}_{29}\text{N}_2\text{O}_4\text{PF}_6\cdot 0.25\text{H}_2\text{O}$: C, 60.83; H, 4.30; N, 4.05. Found: C, 60.85; H, 4.10; N, 4.00. m/z : 541 ($[\text{M} - \text{PF}_6]^+$). Data for crude chloride salt, [2]Cl: δ_{H} (400 MHz, CD_3OD) 8.98 (2 H, d, $J = 7.1$ Hz, $\text{C}_5\text{H}_4\text{N}$), 8.87 (1 H, t, $J = 1.5$ Hz, C_6H_3), 8.64 (2 H, d, $J = 1.5$ Hz, C_6H_3), 8.24 (2 H, d, $J = 7.1$ Hz, $\text{C}_5\text{H}_4\text{N}$), 8.04 (1 H, d, $J = 16.1$ Hz, CH), 7.67 (2 H, d, $J = 8.8$ Hz, C_6H_4), 7.39–7.33 (5 H, Ph + CH), 7.20–7.14 (6 H, Ph), 7.00 (2 H, d, $J = 8.8$ Hz, C_6H_4), 4.02 (6 H, s, 2CO₂Me). $\nu(\text{C}=\text{O})$ 1721s cm^{-1} .

2.3.5. *(E)-4'-(Dimethylamino)-N-(4-methoxycarbonylphenyl)-4-stilbazolium hexafluorophosphate, [3]PF₆*

This compound was prepared in a manner similar to [1]PF₆ by using 4-(dimethylamino)benzaldehyde (125 mg, 0.838 mmol) and [(4-MCPh)pic]Cl•0.8H₂O (100 mg, 0.360 mmol) in place of [(3,5-MC₂Ph)pic⁺]Cl•H₂O to give a dark purple solid. Yield: 109 mg (60%). δ_{H} (400 MHz, CD_3COCD_3) 9.05 (2 H, d, $J = 7.1$ Hz, $\text{C}_5\text{H}_4\text{N}$), 8.33 (2 H, d, $J = 8.6$ Hz, C_6H_4), 8.29 (2 H, d, $J = 7.1$ Hz, $\text{C}_5\text{H}_4\text{N}$), 8.15 (1 H, d, $J = 15.9$ Hz, CH), 8.07 (2 H, d, $J = 8.8$ Hz, C_6H_4), 7.70 (2 H, d, $J = 8.8$ Hz, C_6H_4), 7.35 (1 H, d, $J = 16.1$ Hz, CH), 6.85 (2 H, d, $J = 9.1$ Hz, C_6H_4), 3.97 (3 H, s, CO₂Me),

3.12 (6 H, s, NMe₂). $\nu(\text{C=O})$ 1714s cm⁻¹. Anal. Calcd (%) for C₂₃H₂₃N₂O₂PF₆: C, 54.77; H, 4.60; N, 5.55. Found: C, 54.84; H, 4.46; N, 5.37. m/z : 359 ([M - PF₆]⁺). Data for crude chloride salt, [3]Cl: δ_{H} (400 MHz, CD₃OD) 8.83 (2 H, d, J = 7.1 Hz, C₅H₄N), 8.33 (2 H, d, J = 8.8 Hz, C₆H₄), 8.12 (2 H, d, J = 7.1 Hz, C₅H₄N), 8.02 (1 H, d, J = 15.9 Hz, CH), 7.90 (2 H, d, J = 8.8 Hz, C₆H₄), 7.68 (2 H, d, J = 9.1 Hz, C₆H₄), 7.20 (1 H, d, J = 15.9 Hz, CH), 6.82 (2 H, d, J = 9.1 Hz, C₆H₄), 3.98 (3 H, s, CO₂Me), 3.10 (6 H, s, NMe₂). $\nu(\text{C=O})$ 1715s cm⁻¹.

2.3.6. *(E)-4'-(Diphenylamino)-N-(4-methoxycarbonylphenyl)-4-stilbazolium hexafluorophosphate, [4]PF₆*

This compound was prepared in a manner similar to [3]PF₆ by using 4-(diphenylamino)benzaldehyde (228 mg, 0.834 mmol) in place of 4-(dimethylamino)benzaldehyde to give a dark red solid. Yield: 140 mg (62%). δ_{H} (400 MHz, CD₃COCD₃) 9.16 (2 H, d, J = 7.1 Hz, C₅H₄N), 8.41 (2 H, d, J = 7.1 Hz, C₅H₄N), 8.34 (2 H, d, J = 8.8 Hz, C₆H₄), 8.19 (1 H, d, J = 16.1 Hz, CH), 8.09 (2 H, d, J = 8.8 Hz, C₆H₄), 7.71 (2 H, d, J = 8.8 Hz, C₆H₄), 7.51 (1 H, d, J = 16.1 Hz, CH), 7.43–7.39 (4 H, Ph), 7.23–7.18 (6 H, Ph), 7.00 (2 H, d, J = 8.8 Hz, C₆H₄), 3.97 (3 H, s, CO₂Me). $\nu(\text{C=O})$ 1715s cm⁻¹. Anal. Calcd (%) for C₃₃H₂₇N₂O₂PF₆: C, 63.06; H, 4.33; N, 4.46. Found: C, 62.86; H, 4.18; N, 4.27. m/z : 484 ([M - PF₆]⁺). Data for crude chloride salt, [4]Cl: δ_{H} (400 MHz, CD₃OD) 8.87 (2 H, d, J = 7.1 Hz, C₅H₄N), 8.34 (2 H, d, J = 8.8 Hz, C₆H₄), 8.24 (2 H, d, J = 7.1 Hz, C₅H₄N), 8.04 (1 H, d, J = 16.1 Hz, CH), 7.93 (2 H, d, J = 8.8 Hz, C₆H₄), 7.66 (2 H, d, J = 8.8 Hz, C₆H₄), 7.39–7.33 (5 H, CH + Ph), 7.20–7.15 (6 H, Ph), 7.00 (2 H, d, J = 8.8 Hz, C₆H₄), 3.99 (3 H, s, CO₂Me). $\nu(\text{C=O})$ 1713s cm⁻¹.

2.3.7. *(E)-4'-(Dimethylamino)-N-(3,5-bis(carboxy)phenyl)-4-stilbazolium hexafluorophosphate, [5]PF₆*

The crude chloride salt [1]Cl was prepared exactly as described above, then dissolved in methanol (5 mL) and aqueous NaOH (2%, 1 mL) was added. The

mixture was stirred at room temperature for 7 h and then acidified with concentrated H₂SO₄ (5 drops). Aqueous NH₄PF₆ (1 M) was added and the flask was left in a refrigerator overnight. The dark purple precipitate was filtered off, washed with water and dried. Yield: 33 mg (21%). δ_{H} (400 MHz, CD₃COCD₃) 9.15 (2 H, d, $J = 7.1$ Hz, C₅H₄N), 8.86 (1 H, t, $J = 1.4$ Hz, C₆H₃), 8.69 (2 H, d, $J = 1.3$ Hz, C₆H₃), 8.32 (2 H, d, $J = 6.8$ Hz, C₅H₄N), 8.18 (1 H, d, $J = 15.9$ Hz, CH), 7.71 (2 H, d, $J = 8.8$ Hz, C₆H₄), 7.37 (1 H, d, $J = 15.6$ Hz, CH), 6.85 (2 H, d, $J = 9.1$ Hz, C₆H₄), 3.13 (6 H, s, NMe₂). $\nu(\text{C}=\text{O})$ 1716s cm⁻¹. Anal. Calcd (%) for C₂₃H₂₁F₆N₂O₄P: C, 51.69; H, 3.96; N, 5.24. Found: C, 51.36; H, 4.11; N, 5.11. m/z : 411 ([M - PF₆ + Na]⁺), 389 ([M - PF₆]⁺).

2.3.8. *(E)-4'-(Diphenylamino)-N-(3,5-bis(carboxyphenyl))-4-stilbazolium hexafluorophosphate, [6]PF₆*

The crude chloride salt [2]Cl was prepared exactly as described above, then treated as for [5]PF₆ to give a dark red/purple solid. Purification was effected by reprecipitation from acetone/diethyl ether. Yield: 24 mg (12%). δ_{H} (400 MHz, CD₃COCD₃) 9.24 (2 H, d, $J = 7.1$ Hz, C₅H₄N), 8.84 (1 H, t, $J = 1.5$ Hz, C₆H₃), 8.69 (2 H, d, $J = 1.5$ Hz, C₆H₃), 8.42 (2 H, d, $J = 7.1$ Hz, C₅H₄N), 8.19 (1 H, d, $J = 16.1$ Hz, CH), 7.68 (2 H, d, $J = 8.8$ Hz, C₆H₄), 7.50 (1 H, d, $J = 15.9$ Hz, CH), 7.40–7.36 (4 H, Ph), 7.20–7.15 (6 H, Ph), 6.98 (2 H, d, $J = 8.8$ Hz, C₆H₄). $\nu(\text{C}=\text{O})$ 1713s cm⁻¹. Anal. Calcd (%) for C₃₃H₂₅F₆N₂O₄P•2.3H₂O: C, 56.62; H, 4.26; N, 4.00. Found: C, 56.62; H, 3.96; N, 3.80. m/z : 557 ([M - PF₆ + 2Na]⁺), 535 ([M - PF₆ + Na]⁺), 513 ([M - PF₆]⁺).

2.3.9. *(E)-4'-(Dimethylamino)-N-(4-carboxyphenyl)-4-stilbazolium hexafluorophosphate, [7]PF₆*

The crude chloride salt [3]Cl was prepared exactly as described above, then treated as for [5]PF₆ to give a dark purple solid. Yield: 46 mg (26%). δ_{H} (400 MHz, CD₃COCD₃) 9.06 (2 H, d, $J = 7.1$ Hz, C₅H₄N), 8.35 (2 H, d, $J = 8.8$ Hz, C₆H₄), 8.29 (2 H, d, $J = 7.3$ Hz, C₅H₄N), 8.16 (1 H, d, $J = 15.9$ Hz, CH), 8.06 (2 H, d, $J = 8.8$ Hz,

C₆H₄), 7.71 (2 H, d, $J = 8.8$ Hz, C₆H₄), 7.35 (1 H, d, $J = 15.9$ Hz, CH), 6.85 (2 H, d, $J = 9.1$ Hz, C₆H₄), 3.13 (6 H, s, NMe₂). $\nu(\text{C}=\text{O})$ 1702s cm⁻¹. Anal. Calcd (%) for C₂₂H₂₁F₆N₂O₂P•0.5H₂O: C, 52.91; H, 4.44; N, 5.61. Found: C, 52.84; H, 4.03; N, 5.48. m/z : 367 ([M - PF₆ + Na]⁺), 345 ([M - PF₆]⁺).

2.3.10. *(E)-4'-(Diphenylamino)-N-(4-carboxyphenyl)-4-stilbazolium hexafluorophosphate, [8]PF₆*

The crude chloride salt [4]Cl was prepared exactly as described above, then treated as for [5]PF₆ to give a dark red/purple solid. Purification was effected by reprecipitation from acetone/diethyl ether. Yield: 22 mg (10%). δ_{H} (400 MHz, CD₃COCD₃) 9.19 (2 H, d, $J = 7.1$ Hz, C₅H₄N), 8.43 (2 H, d, $J = 7.2$ Hz, C₅H₄N), 8.36 (2 H, d, $J = 8.7$ Hz, C₆H₄), 8.20 (1 H, d, $J = 16.1$ Hz, CH), 8.10 (2 H, d, $J = 8.8$ Hz, C₆H₄), 7.71 (2 H, d, $J = 8.3$ Hz, C₆H₄), 7.52 (1 H, d, $J = 16.1$ Hz, CH), 7.43–7.39 (4 H, Ph), 7.23–7.19 (6 H, Ph), 7.01 (2 H, d, $J = 8.3$ Hz, C₆H₄). $\nu(\text{C}=\text{O})$ 1707s cm⁻¹. Anal. Calcd (%) for C₃₂H₂₅F₆N₂O₂P•0.7H₂O: C, 61.29; H, 4.24; N, 4.47. Found: C, 61.34; H, 4.13; N, 4.49. m/z : 483 ([M - PF₆ + Na]⁺), 469 ([M - PF₆]⁺).

2.4. *X-ray crystallographic studies*

Crystals of the salts [(4-MCPh)pic⁺]Cl and [(3,5-MC₂Ph)pic⁺]Cl•EtOH were grown by vapour diffusion of diethyl ether into ethanol solutions, while those of [1]PF₆, [2]PF₆•MeCN, and [4]PF₆•MeCN were obtained similarly with acetonitrile solutions. Data were collected on a Bruker APEX II CCD X-ray diffractometer by using MoK_α radiation ($\lambda = 0.71073$ Å), and the data were processed by using the Bruker SAINT and SADABS [8] software packages. The structures were solved by direct methods using SHELXS-97 [9], and refined by full-matrix least-squares on all F_0^2 data using SHELXL-97 [10]. All non-hydrogen atoms were refined anisotropically and hydrogen atoms were included in idealized positions using the riding model, with thermal parameters of 1.2 times those of aromatic parent carbon

atoms, and 1.5 times those of methyl parent carbons. The crystal of [(4-MCPh)pic⁺]Cl was a weakly diffracting needle, so the data were cut at 0.9 Å resolution. The asymmetric unit of [1]PF₆ contains two cations and two PF₆⁻ anions with a disordered solvent fragment that could not be identified, but is presumably diethyl ether; all atoms of this group were defined as C at 0.5 occupancy and refined isotropically. For this structure, the phenyl rings were constrained to be regular hexagons, and restraints were also applied to the geometry of the pyridyl group. The crystal was very weakly diffracting and so the data were cut at 1.2 Å resolution. The crystals of [4]PF₆•MeCN were also extremely weakly diffracting, so the data were cut at 1 Å resolution. In this case, the asymmetric unit contains two cations, two PF₆⁻ anions and two acetonitrile molecules. The atoms C36–C53 are disordered over two sites, and the two components of the disordered phenyl group were constrained to be regular hexagons. All other calculations were carried out by using the SHELXTL package [11]. Crystallographic data and refinement details are presented in Table 1.

The CCDC depositions 809929 ([4-MCPh)pic⁺]Cl), 809930 ([3,5-MC₂Ph)pic⁺]Cl•EtOH), 809931 ([1]PF₆), 809932 ([2]PF₆•MeCN) and 809933 ([4]PF₆•MeCN) contain the supplementary crystallographic data for this paper. These data can be obtained free of charge via www.ccdc.cam.ac.uk/data_request/cif, data_request@ccdc.cam.ac.uk, or by contacting The Cambridge Crystallographic Data Centre, 12, Union Road, Cambridge CB2 1EZ, UK; fax: +44 1223 336033.

2.5. Theoretical calculations

Structure optimizations (B3LYP/6-311g*) [12,13] and time-dependent density functional theory calculations were carried out by using the Gaussian 03 software package [14]. The first 50 excited states were calculated in each case. The conductor-like polarizable continuum model (CPCM) [15] was employed to take account of the effect of acetonitrile on chromophore **6**. When using the crystal structure geometry, all counterions and solvent molecules were removed and methyl

groups (on the esters) were replaced with protons (bond distance between O and H modified to 1.00 Å). The UV–vis absorption spectra were simulated by using the GaussSum program [16].

2.6. Fabrication of dye-sensitized solar cells

TiO₂-based cells were fabricated as follows. Fluorine-doped tin oxide (FTO) glass (TEC15, Libbey Owens Ford) was cleaned by successive sonication for 15 min in aqueous detergent, acetone, isopropanol and ethanol. A thin compact layer (60 nm) of TiO₂ was then deposited on the cleaned FTO by spray pyrolysis. The mesoporous layers were prepared by doctor-blading a commercial TiO₂ paste (Dyesol, DSL-18-NR) onto the coated FTO substrates. The film was dried at 80 °C on a hotplate for 15 min and then sintered at 500 °C for 30 min to burn out the organic binder, leaving the mesoporous anatase structure of thickness around 13 μm. After cooling to about 100 °C, the films were immersed into 5 × 10⁻⁴ M solutions of the test dyes in acetonitrile and left for 16 h. Chenodeoxycholic acid (10⁻³ M) was added in the dye bath to reduce dye aggregation on the TiO₂ film. The dye-coated film was washed thoroughly with HPLC grade acetonitrile and then dried under nitrogen. The cells were assembled by sealing the dye-coated electrodes to thermally platinized FTO (TEC8) counter electrodes using a 25 μm thermoplastic gasket (Surlyn) at 80 °C under pressure. The narrow gap between the two electrodes was vacuum filled with electrolyte via holes predrilled in the counter electrode. The filling holes were sealed with microscope slip using Surlyn. The active area of the cells was 1 cm². **Hongxia to confirm.**

Two types of electrolyte were used in the TiO₂-based cells. Electrolyte A was composed of 0.06 M I₂, 0.6 M 1-propyl-3-methylimidazolium iodide (PMII, Merck), 0.2 M NaI, 0.1 M guanidinium thiocyanate (GuSCN) and 0.5 M *tert*-butylpyridine (TBP) in 3-methoxypropionitrile (MPN). Electrolyte B (sodium free) was composed of 0.03 M I₂, 0.6 M PMII, 0.1 M GuSCN and 0.5 M TBP in acetonitrile/valeronitrile

(85:15 v/v). All of the chemicals used in the cell fabrication were obtained from Sigma-Aldrich unless stated otherwise.

ZnO-based cells were fabricated as follows. The ZnO paste was prepared by using a 1:1 mixture of two commercial ZnO powders, Evonik VP AdNano@ZnO20 (particle size ca. 20 nm) and PI-KEM (particle size ca. 50 nm). For thin film preparation the mixture was dispersed in water and ethanol (30:70) and stirred overnight to obtain a colloidal suspension of 30 wt. This suspension was spread onto previously cleaned FTO glass (TEC15, Hartford Glass Co) with a glass rod using Scotch tape as spacer, and the film was then heated at 420 °C for 30 min. The ZnO substrates were coated with the test dyes in similar manner to the TiO₂ films, but using an immersion time of only 30 min. A photoanode coated with the reference dye D149 (Mitsubishi Paper Mills Limited) was prepared similarly, but using 7×10^{-4} M chenodeoxycholic in *tert*-butyl alcohol/acetonitrile (1:1). The counter electrode was prepared by spreading 15 μ l of *platisol* (Solaronix) on the conductive side of TEC8 electrodes and subsequent annealing at 400 °C for 5 min. Cells with an active area of 0.81 cm² were assembled exactly as those containing the TiO₂ films.

Five different electrolyte solutions were tested in the ZnO-based cells with the dye salt [7]PF₆: (1) 0.5 M LiI, 0.05 M I₂, 0.5 M TBP in MPN; (2) 5×10^{-5} M I₂, 0.5 M TBAI in acetonitrile/ethylencarbonate (1:4); (3) 0.5 M LiI, 0.03 M I₂, 0.5 M TBP, 0.1 M GuSCN in acetonitrile; (4) 0.03 M I₂, 0.6 M PMII, 0.1 M GuSCN, 0.5 M TBP in acetonitrile; (5) 0.06 M I₂, 0.6 M PMII, 0.2 M NaI, 0.1 M GuSCN, 0.5 M TBP in MPN. Electrolyte 2 gave the best cell performance, so data were obtained for [8]PF₆ in only this electrolyte.

2.7. Current-voltage measurements

The current-voltage characteristics of the TiO₂-based cells were measured using a solar simulator (Müller) equipped with 1 kW xenon lamp. The intensity of the illumination was calibrated with a standard silicon reference cell (Fraunhofer ISE) to

provide 1 sun (100 mW cm^{-2}). AM1.5 and KG5 filters were used to minimize the mismatch between the solar simulator and the AM1.5 solar spectrum. The current voltage plots were recorded using a computer-controlled system (Whistonbrook).

The ZnO-based cells were characterized with a solar simulator (ABET) combined with a AM1.5G filter. A reference cell with temperature output (Oriel, 91150) was used for calibrate the illumination output to 1 sun. Photocurrents, photovoltages and current-voltage curves were measured by using a 2400 Keithley SourceMeter.

2.8. Incident-photon-to-electron conversion efficiency (IPCE) measurements

The IPCE of the TiO_2 -based cells was measured with a home-made setup. Illumination was provided by a tungsten lamp in combination with a monochrometer (Bentham, England). A yellow filter was employed at wavelengths above 550 nm to eliminate second-order diffracted light, and no bias illumination was used. The number of photons at each wavelength was calculated by a calibrated photodiode (SD-112 UV), and the electron generated by the cell at each wavelength was recorded by a potentiostat (SR 850, Stanford Research System).

Table 1

Crystallographic data and refinement details for the salts [(4-MCPh)pic⁺]Cl, [(3,5-MC₂Ph)pic⁺]Cl•EtOH, [1]PF₆, [2]PF₆•MeCN and [4]PF₆•MeCN.

	[(4-MCPh)pic ⁺]Cl	[(3,5-MC ₂ Ph)pic ⁺]Cl•EtOH	[1]PF ₆	[2]PF ₆ •MeCN	[4]PF ₆ •MeCN
formula	C ₁₄ H ₁₄ ClNO ₂	C ₁₈ H ₂₂ ClNO ₅	C ₅₆ H ₅₀ F ₁₂ N ₄ O ₈ P ₂	C ₃₇ H ₃₂ F ₆ N ₃ O ₄ P	C ₃₅ H ₃₀ F ₆ N ₃ O ₂ P
<i>M</i> _w	263.71	367.82	1196.94	727.63	669.59
cryst syst	orthorhombic	monoclinic	triclinic	triclinic	triclinic
space group	<i>Fdd2</i>	<i>P2/c</i>	<i>P</i> $\bar{1}$	<i>P</i> $\bar{1}$	<i>P</i> $\bar{1}$
<i>a</i> (Å)	28.673(15)	12.232(2)	6.914(9)	8.0011(16)	9.832(7)
<i>b</i> (Å)	42.40(2)	6.7253(12)	11.460(14)	10.175(2)	10.682(7)
<i>c</i> (Å)	4.232(2)	23.092(4)	17.32(2)	21.333(4)	29.87(2)
<i>α</i> (deg)	90	90	84.56(2)	99.113(4)	81.414(13)
<i>β</i> (deg)	90	102.791(3)	84.58(2)	95.656(4)	86.504(13)
<i>γ</i> (deg)	90	90	87.50(2)	96.570(3)	76.879(12)
<i>U</i> (Å ³)	5145(5)	1852.6(6)	1359(3)	1691.4(6)	3020(4)
<i>Z</i>	16	4	1	2	4
<i>D</i> _{calcd} (Mg m ⁻³)	1.362	1.319	1.463	1.429	1.473
<i>T</i> (K)	100(2)	100(2)	100(2)	100(2)	100(2)
<i>μ</i> (mm ⁻¹)	0.290	0.233	0.180	0.160	0.167
crystal size (mm)	0.80 × 0.02 × 0.02	0.33 × 0.30 × 0.25	0.60 × 0.10 × 0.05	0.75 × 0.15 × 0.05	0.60 × 0.10 × 0.04
crystal appearance	colourless needle	orange block	red plate	red plate	red plate
no. of reflns collected	7750	13878	3952	10448	10926
no. of independent reflns (<i>R</i> _{int})	1844 (0.1909)	3774 (0.0835)	1650 (0.1961)	4838 (0.0596)	6256 (0.1265)
<i>θ</i> _{max} (deg) (completeness)	23.25 (99.9%)	25.00 (99.7%)	17.22 (99.9%)	23.26 (99.7%)	20.81 (98.9%)
reflns with <i>I</i> > 2σ(<i>I</i>)	1127	2387	820	3850	2927
GOF on <i>F</i> ²	0.914	1.020	1.107	1.135	0.873
final <i>R</i> 1, <i>wR</i> 2 [<i>I</i> > 2σ(<i>I</i>)]	0.0762, 0.1286	0.0695, 0.1313	0.1434, 0.3187	0.0713, 0.1443	0.0700, 0.0947
(all data)	0.1278, 0.1468	0.1169, 0.1481	0.2254, 0.3658	0.0925, 0.1534	0.1586, 0.1158
peak and hole (e Å ⁻³)	0.340, -0.277	0.678, -0.880	0.675, -0.334	0.951, -0.412	0.294, -0.309

3. Results and discussion

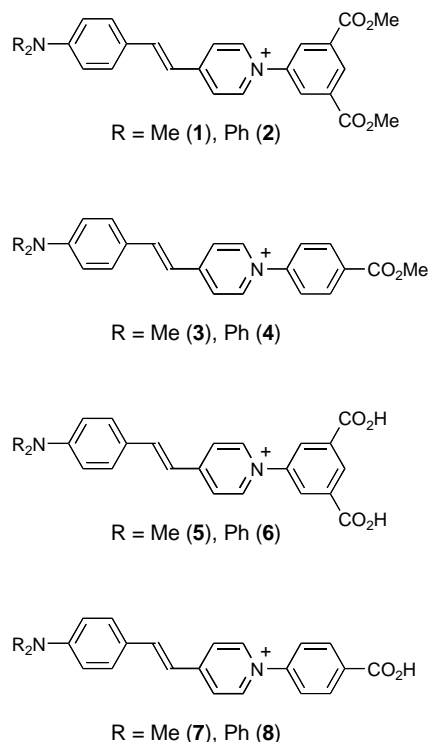


Fig. 1. Chemical structures of the stilbazolium cations investigated; all were isolated and studied as their PF_6^- salts.

3.1. Synthesis and characterization

We have previously investigated salts of a number of *N*-arylstilbazolium cations as materials for nonlinear optics [5]. These studies have confirmed the strong electron-accepting nature of the pyridinium groups in such molecules, revealing intense ICT absorptions in the visible region that may be exploitable in DSSCs. The new cations **1–4** were synthesized by using an established method that involves Knoevenagel condensation of an aldehyde with a picolinium derivative. The required new chloride salt precursors $[(3,5\text{-MC}_2\text{Ph})\text{pic}^+]\text{Cl}$ and $[(4\text{-MCPH})\text{pic}^+]\text{Cl}$ were prepared via Zincke-type reactions with $[\text{dnppic}^+]\text{Cl}$ [5a], and isolated in moderate yields after column chromatography on silica gel.

The IR spectra of the new compounds all show relatively intense $\nu(\text{C}=\text{O})$ stretching bands, together with various other absorptions, most notably those due to the PF_6^- anions in $[\mathbf{1-8}]\text{PF}_6$ (a very intense band due to a stretching mode at ca. 835–840 cm^{-1} , together with a sharper but somewhat less intense band at ca. 560 cm^{-1} due to a bending mode). The energies of the $\nu(\text{C}=\text{O})$ bands show several general trends: (i) replacing $\text{R} = \text{Me}$ with Ph has little effect; (ii) the disubstituted species always have higher $\nu(\text{C}=\text{O})$ values (by 6–17 cm^{-1}) when compared with their monosubstituted analogues; (iii) ester hydrolysis lowers $\nu(\text{C}=\text{O})$ by 8–17 cm^{-1} .

3.2. Electronic absorption spectroscopy

UV–vis absorption data for $[\mathbf{1-8}]\text{PF}_6$ in acetonitrile are presented in Table 2, and representative spectra of $[\mathbf{3}]\text{PF}_6$ and $[\mathbf{4}]\text{PF}_6$ are shown in Figure 2. These spectra are dominated by intense $\pi \rightarrow \pi^*$ ICT bands in the visible region and also one or more less intense bands due to $\pi \rightarrow \pi^*$ transitions having limited directional nature at higher energies.

In each case, replacing $\text{R} = \text{Me}$ with Ph causes the ICT E_{max} value to increase by ca 0.1 eV (Figure 2). This trend reflects the weaker π -electron donating strength of the diarylamino group derived by Kwon *et al.* by using density functional theory (DFT)-calculated bond distances and ^{13}C NMR chemical shifts [17]. The ICT band intensities show little sensitivity to the nature of the electron donor group. The spectra are not significantly affected either by hydrolysis of the ester groups or by varying the substitution pattern on the phenyl ring attached to the pyridyl group.

Table 2UV-vis absorption and electrochemical data for salts [1–8]PF₆ in acetonitrile.

salt	λ_{\max} , nm (ϵ , $10^3 \text{ M}^{-1} \text{ cm}^{-1}$) ^a	E_{\max} , eV ^a	assignment	E , V vs Ag–AgCl (ΔE_p , mV) ^b		
				E_{pa} ^d	oxidation $E_{1/2}$	reduction ^c
[1]PF ₆	276 (11.7)	4.49	$\pi \rightarrow \pi^*$	0.92		–0.79
	307 (10.7)	4.04	$\pi \rightarrow \pi^*$			
	518 (51.2)	2.39	ICT			
[2]PF ₆	279sh (18.5)	4.44	$\pi \rightarrow \pi^*$	1.09	1.04 (100)	–0.74
	303 (23.2)	4.09	$\pi \rightarrow \pi^*$			
	502 (54.5)	2.47	ICT			
[3]PF ₆	276 (12.7)	4.49	$\pi \rightarrow \pi^*$	0.92		–0.79
	310 (13.0)	4.00	$\pi \rightarrow \pi^*$			
	519 (54.9)	2.39	ICT			
[4]PF ₆	279sh (20.1)	4.44	$\pi \rightarrow \pi^*$	1.09	1.04 (100)	–0.73
	305 (23.4)	4.07	$\pi \rightarrow \pi^*$			
	502 (53.6)	2.47	ICT			
[5]PF ₆	276 (8.63)	4.49	$\pi \rightarrow \pi^*$	0.96		–0.80
	310 (9.21)	4.00	$\pi \rightarrow \pi^*$			
	516 (41.5)	2.40	ICT			
[6]PF ₆	278sh (16.5)	4.46	$\pi \rightarrow \pi^*$	1.04	1.02 (60)	–0.71
	303 (22.0)	4.09	$\pi \rightarrow \pi^*$			
	500 (44.7)	2.48	ICT			
[7]PF ₆	276 (8.54)	4.49	$\pi \rightarrow \pi^*$	0.93		–0.79
	310 (9.27)	4.00	$\pi \rightarrow \pi^*$			
	516 (44.5)	2.40	ICT			
[8]PF ₆	278sh (16.8)	4.46	$\pi \rightarrow \pi^*$	1.08	1.04 (80)	–0.72
	304 (22.2)	4.08	$\pi \rightarrow \pi^*$			
	498 (41.9)	2.49	ICT			

^a Solutions *ca.* 10^{-5} M. ^b Solutions *ca.* 10^{-3} M in analyte and 0.1 M in [NBu₄]ⁿPF₆; potentials quoted at a scan rate of 200 mV s⁻¹ and using a glassy carbon working electrode. Ferrocene internal reference $E_{1/2} = 0.45$ V, $\Delta E_p = 80$ mV. ^c E_{pc} for an irreversible process. ^d For an irreversible process.

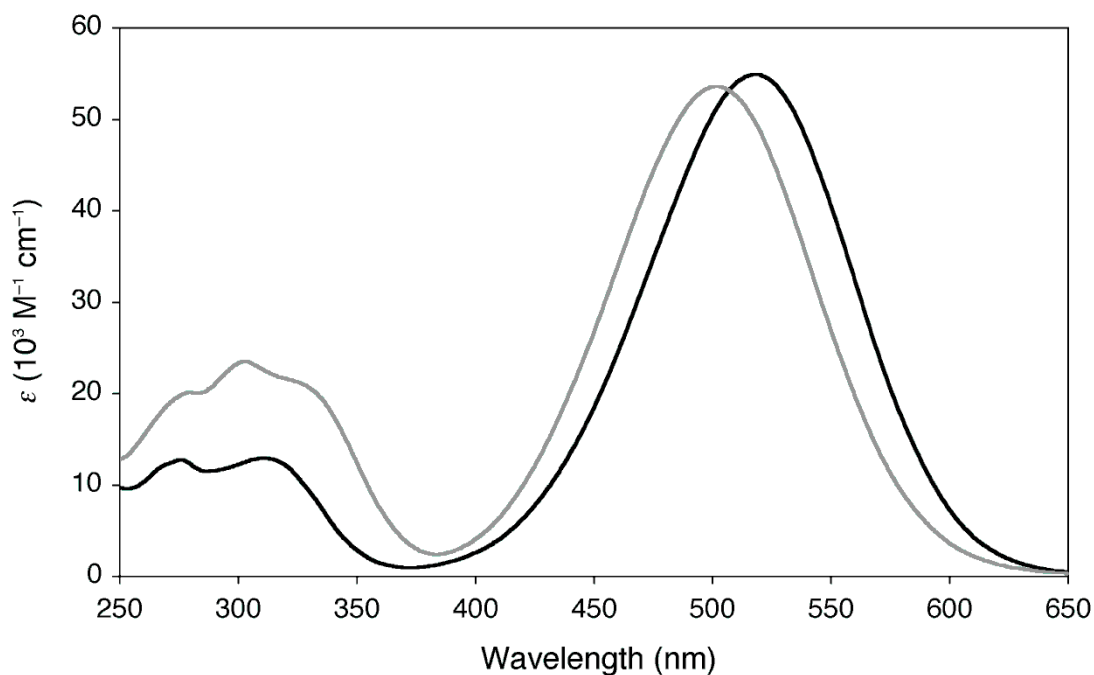


Fig. 2. UV-vis absorption spectra of [3]PF₆ (black) and [4]PF₆ (gray) at 293 K in acetonitrile.

3.3. Electrochemistry

Cyclic voltammetric data for [1–8]PF₆ in acetonitrile are presented in Table 2, and representative voltammograms of [1]PF₆ and [2]PF₆ are shown in Figure 3. Each compound shows a single process attributable to one-electron oxidation of the HOMO, presumably located primarily on the phenylamino substituent, at ca. 1 V vs Ag–AgCl; these processes are irreversible when R = Me, but reversible when R = Ph (Figure 3). This difference is likely attributable to delocalization, and hence stabilization, of the positive charge over the phenyl rings in the –NPh₂ derivatives. The E_{pa} values for the latter are always somewhat higher than those for their –NMe₂ analogues, in keeping with the stronger relative electron donating ability of the dimethylamino group (see above). In each case, an irreversible wave is also observed due to one-electron reduction of the LUMO, presumably located largely on the pyridinium moiety, with $E_{pc} \approx -(0.7–0.8)$ V vs Ag–AgCl. Similar behaviour is found

with related stilbazolium derivatives [5], and the irreversible nature of these processes is attributable to the presence of the ethenylene units which can readily engage in chemical reactions upon reduction. Small increases in E_{pc} (50–90 mV) on replacing Me with Ph in the new compounds show that the reduction occurs more readily when the weaker electron donor group is present, *i.e.* the LUMO becomes stabilized.

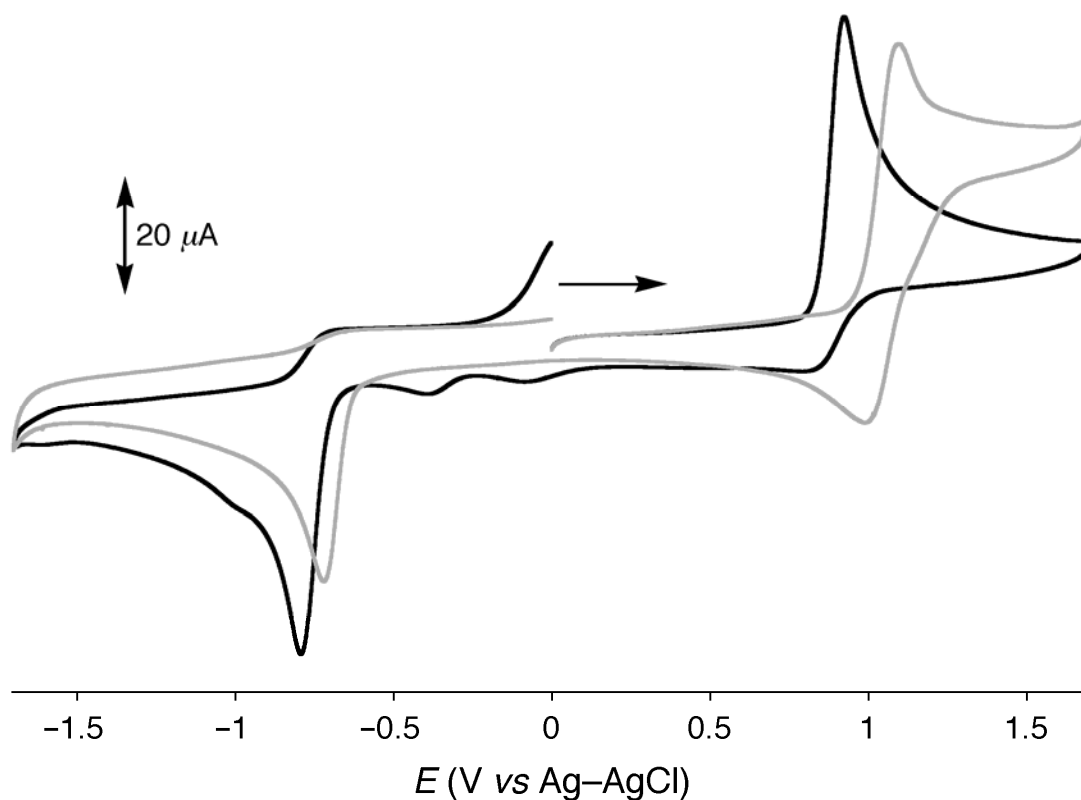


Fig. 3. Cyclic voltammograms for [1]PF₆ (black) and [2]PF₆ (gray) recorded at 200 mV s⁻¹ in acetonitrile with a glassy carbon working electrode. The arrow indicates the direction of the initial scans.

3.4. X-ray crystallography

Representations of the molecular structures of the salts [(4-MCPh)pic⁺]Cl, [(3,5-MC₂Ph)pic⁺]Cl•EtOH, [1]PF₆, [2]PF₆•MeCN and [4]PF₆•MeCN are shown in Figures 4–8. Given that these structures show geometric parameters that are generally

similar to those found in related compounds [1,8,9], further detailed discussion is unnecessary. The dihedral angles between the pyridyl and phenyl ring in [(4-MCPh)pic⁺]Cl and [(3,5-MC₂Ph)pic⁺]Cl•EtOH are *ca.* 39.5° and 48.5°, while the corresponding twists in [1]PF₆, [2]PF₆•MeCN and [4]PF₆•MeCN are *ca.* 31.2°, 44.8° and 34.2/38.6° (two independent cations), respectively. As expected, the increased π -conjugation and lack of steric hindrance leads to smaller dihedral angles between the two aryl rings of the stilbazolium fragments; *ca.* 25.0°, 8.7° and 31.3/29.5° in [1]PF₆, [2]PF₆•MeCN and [4]PF₆•MeCN, respectively.

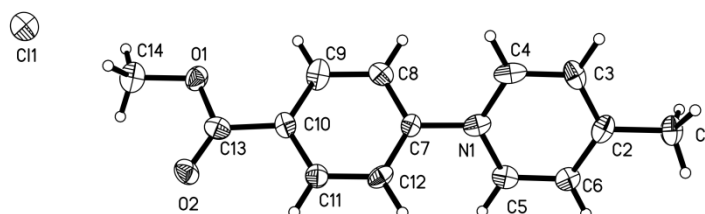


Fig. 4. Representation of the molecular structure of [(4-MCPh)pic⁺]Cl (50% probability ellipsoids).

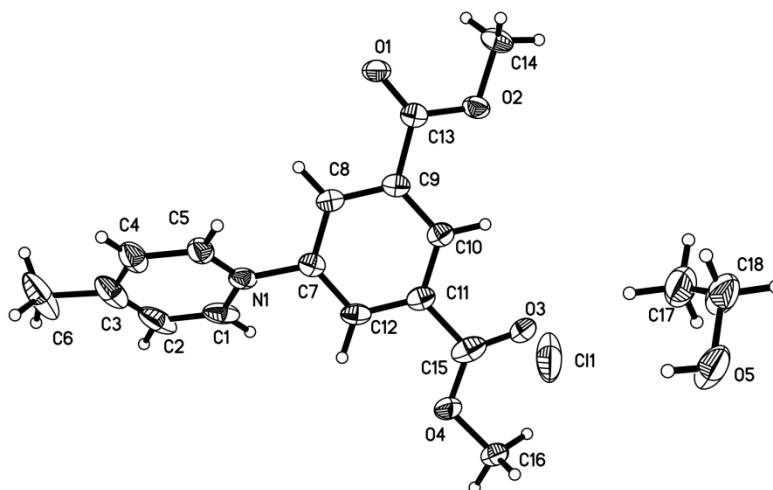


Fig. 5. Representation of the molecular structure of [(3,5-MC₂Ph)pic⁺]Cl•EtOH (50% probability ellipsoids).

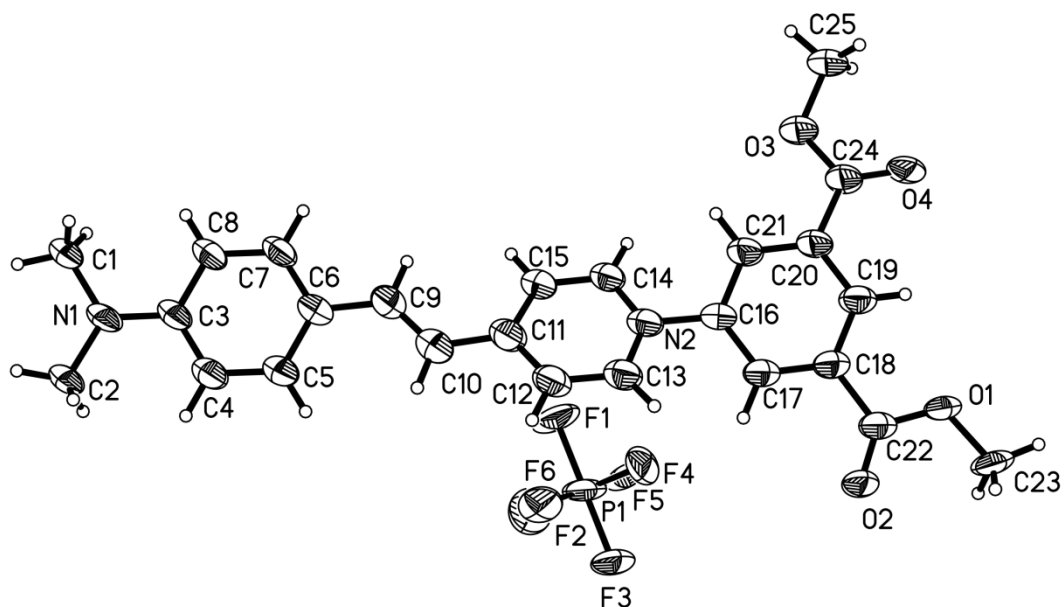


Fig. 6. Representation of the molecular structure of [1]PF₆ (50% probability ellipsoids).

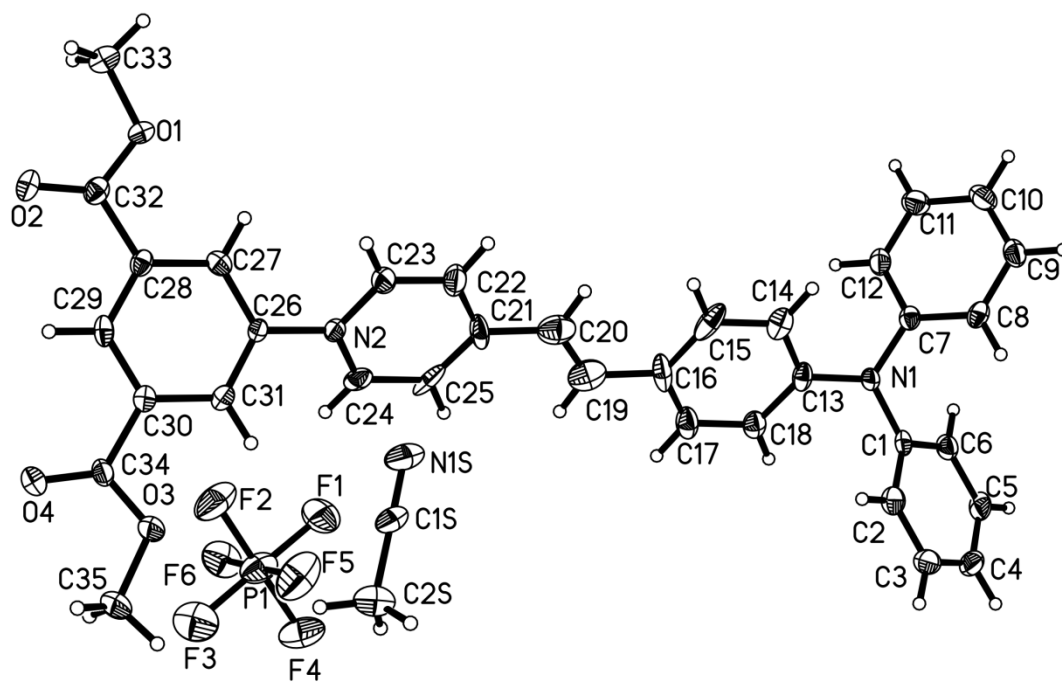


Fig. 7. Representation of the molecular structure of [2]PF₆•MeCN (50% probability ellipsoids).

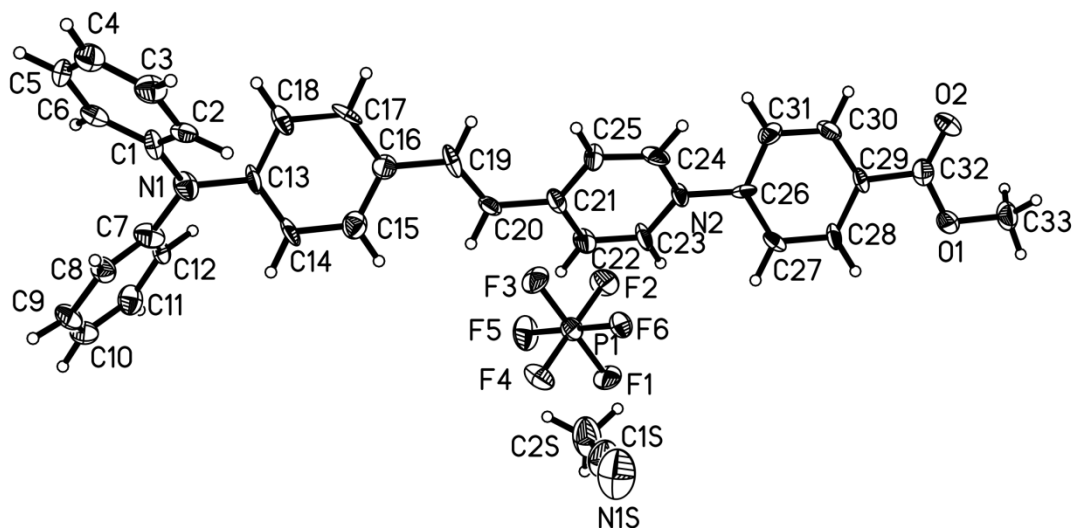


Fig. 8. Representation of the molecular structure of $[4]PF_6 \cdot MeCN$, excluding the disordered cation and associated PF_6^- and MeCN molecules (50% probability ellipsoids).

3.5. Theoretical studies

In order to rationalize the electronic structures and optical properties of the new chromophores, time-dependent DFT (TD-DFT) calculations were carried out by using Gaussian 03 [14]. The predicted transition energies and other details are presented in Table 3. The UV–vis spectra were simulated by using GaussSum [15], and selected spectra are shown in Figures 9 and 10.

Table 3Data from TD-DFT (B3LYP/6-311g*) calculations on the cations **5–8**.

cation	ΔE , eV	f_{os}	major contributions	μ_{12} , D
5^a	2.30	1.14	HOMO \rightarrow LUMO	11.44
	3.52	0.23	HOMO-2 \rightarrow LUMO	4.17
	3.71	0.30	HOMO \rightarrow LUMO+3	4.63
			HOMO-2 \rightarrow LUMO	
			HOMO \rightarrow LUMO+3	
6^a	1.67	0.84	HOMO \rightarrow LUMO	11.53
	3.07	0.23	HOMO-4 \rightarrow LUMO	4.42
	3.14	0.40	HOMO \rightarrow LUMO+3	5.76
			HOMO-4 \rightarrow LUMO	
			HOMO \rightarrow LUMO+3	
6^b	2.20	1.41	HOMO \rightarrow LUMO	12.99
	3.07	0.25	HOMO-1 \rightarrow LUMO	4.63
	3.28	0.37	HOMO-3 \rightarrow LUMO	5.49
6^c	2.29	1.66	HOMO \rightarrow LUMO	13.82
	3.42	0.34	HOMO-1 \rightarrow LUMO	5.09
			HOMO \rightarrow LUMO+2	
7^b	2.56	1.59	HOMO \rightarrow LUMO	12.78
	3.59	0.08	HOMO \rightarrow LUMO+1	2.44
			HOMO \rightarrow LUMO+2	
	3.82	0.20	HOMO-1 \rightarrow LUMO	3.68
8^a	1.71	0.85	HOMO \rightarrow LUMO	11.47
	3.06	0.30	HOMO-3 \rightarrow LUMO	5.09
			HOMO \rightarrow LUMO+2	
	3.19	0.43	HOMO-4 \rightarrow LUMO	5.98
			HOMO-3 \rightarrow LUMO	
		HOMO \rightarrow LUMO+2		

^a Obtained by using the atomic coordinates from the X-ray crystal structure of the corresponding ester derivative. ^b Obtained by using the atomic coordinates from the B3LYP/6-311g*-optimized structure. ^c Obtained by using both the atomic coordinates from the B3LYP/6-311g*-optimized structure and the CPCM (acetonitrile).

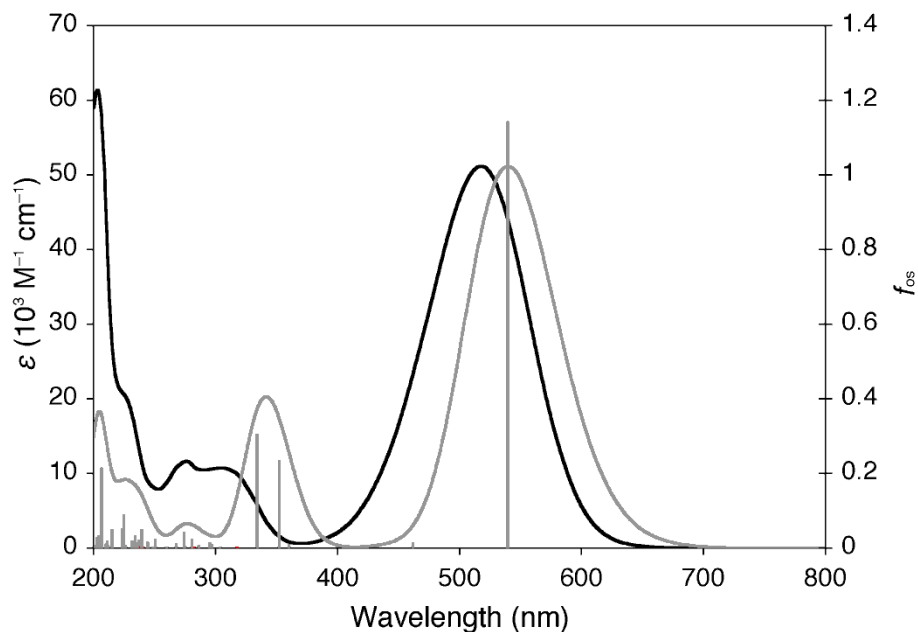


Fig. 9. TD-DFT-calculated (gray) and experimental (black) UV-vis spectra of chromophore **5** and $[5]PF_6$, the latter recorded in acetonitrile. The calculations used the crystal structure geometry determined for the corresponding ester (in $[1]PF_6$). The ϵ -axes refer to the experimental data only and the vertical axes of the calculated data are scaled to match the main experimental absorptions. The oscillator strength axes refer to the individual calculated transitions (vertical gray lines).

For the $-NMe_2$ -substituted cation **5**, using the crystal structure geometry determined for the corresponding ester (in $[1]PF_6$, see above) gave an adequate fit with the observed UV-vis spectrum (Figure 9). In the case of the related monosubstituted cation **7**, no directly relevant crystallographic data are available, so the structure was optimized before the TD-DFT calculations were carried out. For the $-NPh_2$ -substituted chromophores, the calculations produced less consistent results. For **6**, using the crystal structure geometry determined for the corresponding ester (in $[2]PF_6 \cdot MeCN$, see above) gave a very poor fit with the observed UV-vis spectrum (Figure 10a). Therefore, the structure was optimized and the TD-DFT calculations repeated, giving a better match between the predicted and observed spectra. Additional inclusion of an acetonitrile solvent continuum (CPCM) further improves

the agreement with the experimental spectrum (Figure 10b). In the case of **8**, using the crystallographic coordinates for [4]PF₆•MeCN also gave relatively inaccurate results, but geometry optimization has not been performed with this molecule. Optimization of **6** alters the geometry when compared with the related crystal structure. The stilbazole portion is flattened out slightly to become almost perfectly planar, while the dihedral angles between this fragment and the acid-substituted phenyl ring and between the *N*-phenyl and phenylene rings increase. Similar differences are evident between the crystallographic model and optimized structures of **7**.

In all cases, the lowest energy absorption band is confirmed to be a HOMO → LUMO transition with a large transition dipole moment μ_{12} . Inspection of the frontier orbitals (Figure 11) shows that the HOMOs reside mainly on the aminophenyl and ethenylene groups, with some contribution from the pyridyl rings. The LUMOs are spread across the whole molecule, but with major contributions from the pyridyl rings and ethenylene units. The low energy transitions therefore have the expected ICT character. The higher energy band is in all cases calculated to be made up of two separate transitions, and the intensities of these relative to the main band vary somewhat. The ICT energies predicted via TD-DFT when using the crystal structure geometries are lower than the experimental values (Tables 2 and 3). Such differences are commonly found when using TD-DFT to study states with significant ICT character, as noted in other studies relevant to DSSCs [3c]. This underestimation of the excitation energy is reasonable for **5** (0.10 eV) but very large for **6** (0.81 eV) and **8** (0.78 eV). While optimization of the structure for **6** and inclusion of the CPCM produces a closer match between the calculated ΔE and the experimental E_{\max} value, this energy is still underestimated by 0.19 eV. Studies by Liu *et al.* with arylfluorene derivatives having two -NPh₂ substituents underestimated ΔE to a similar extent (ca. 0.2–0.4 eV) at the B3LYP/6-31G(d) level of theory [18]. Such discrepancies may be attributable to a neglect of solvation effects, but other factors may also be important. In contrast, geometry optimization for **7** gives an *overestimation* of the excitation energy, with ΔE being larger than E_{\max} by 0.16 eV.

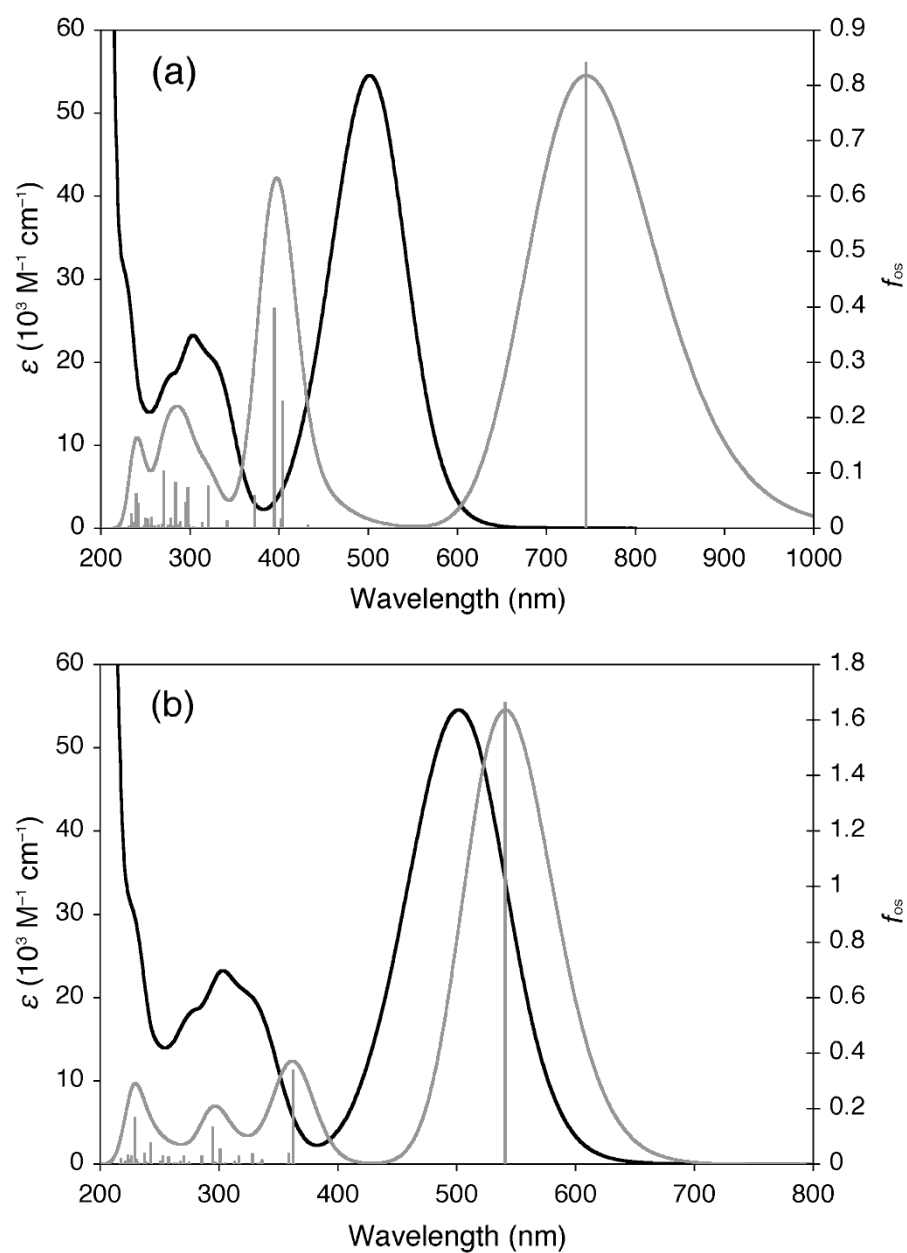


Fig. 10. TD-DFT-calculated (gray) and experimental (black) UV-vis spectra of **6** and $[6]PF_6$, the latter recorded in acetonitrile. The calculations used (a) the crystal structure geometry for the corresponding ester (in $[2]PF_6 \cdot MeCN$), and (b) the B3LYP/6-311g*-optimized structure with CPCM. All other details as for Figure 9.

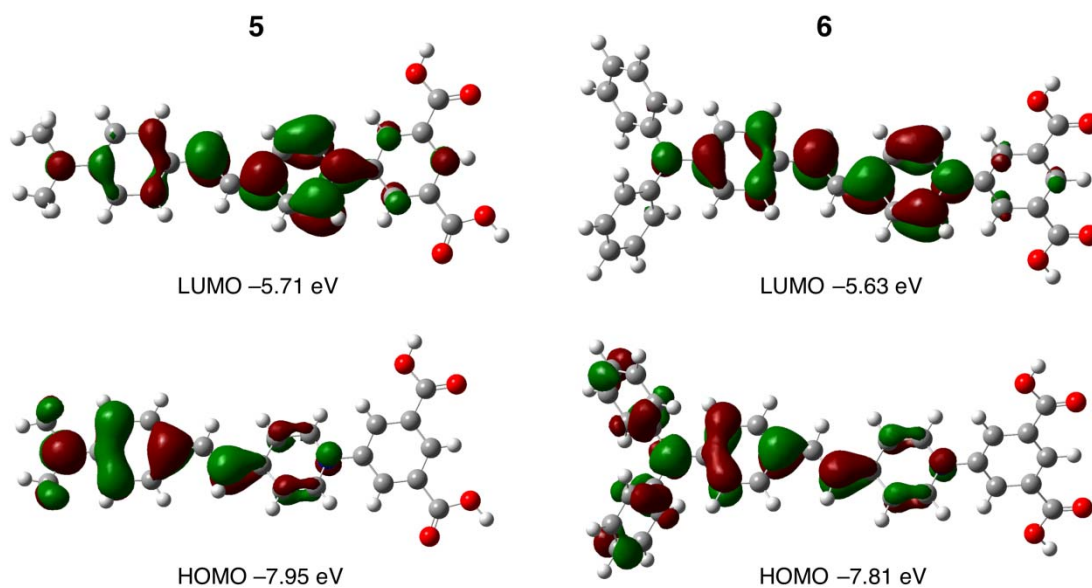


Fig. 11. TD-DFT-derived depictions of the main orbitals involved in the ICT transitions in **5** (using the X-ray crystal structure of the corresponding ester) and **6** (using the B3LYP/6-311g*-optimized structure) (isosurface value 0.03 au).

3.6. Sensitized solar cell studies

The basic physics and chemistry of DSSCs have been reviewed elsewhere,^{1d,19,20} including the derivations of key expressions used here.^{1d}

The carboxylate-functionalized dye salts [**5–8**] PF_6 were tested initially in liquid electrolyte cells with TiO_2 photoanodes. Plots showing the I-V performance of these cells using electrolyte A are depicted in Figure 12, and the AM 1.5 characteristics of the cells together with information on the LUMO energy levels of the dyes are summarized in Table 4.

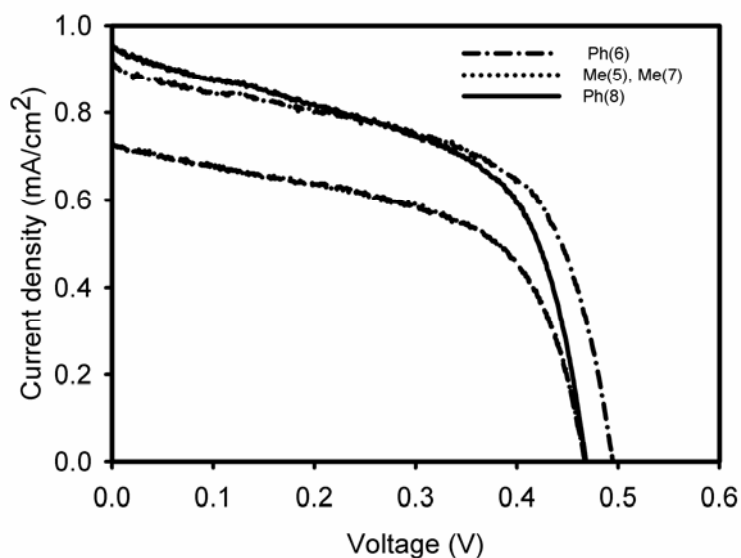


Fig. 12. AM 1.5 Current density-voltage characteristics of TiO₂-based DSSCs fabricated by using salts [5–8]PF₆ with electrolyte A.

Table 4

Current/voltage characteristics of TiO₂-based DSSCs containing [5–8]PF₆ with electrolyte A and the measured and calculated LUMO energies.

salt	J_{SC} (mA cm ⁻²)	V_{OC} (mV)	FF (%)	η (%)	LUMO (V) ^a	LUMO (eV) ^b
[5]PF ₆	0.729	467	56.7	0.193	-0.80	-5.71
[6]PF ₆	0.916	493	59.3	0.268	-0.71	-5.80
[7]PF ₆	0.731	467	57.1	0.195	-0.79	-5.66
[8]PF ₆	0.954	467	55.7	0.248	-0.72	-5.74

^a Measured via cyclic voltammetry in acetonitrile (V vs Ag–AgCl). ^b Obtained by using TD-DFT (B3LYP/6-311g*) calculations on the cation with the atomic coordinates from the X-ray crystal structure of the corresponding ester derivative for all except **7** for which the B3LYP/6-311g*-optimized geometry was used.

The cells containing [5]PF₆, [7]PF₆ and [8]PF₆ give the same open-circuit voltage ($V_{OC} = 467$ mV), while [6]PF₆ gives a value higher by 26 mV (Table 4). The excess electron density $n_{light} - n_{dark}$ under illumination and hence the V_{OC} of a DSSC is determined by the balance between electron injection from the photoexcited sensitizer

and back electron-transfer from the TiO_2 to the oxidized component of the Γ/I_3^- redox couple. For the usual case where $n_{\text{light}} \gg n_{\text{dark}}$, the electron density under open-circuit conditions and first-order back electron-transfer is given by

$$n_{\text{light}} = \frac{\eta_{\text{LH}} \eta_{\text{inj}} I_0 \tau}{d} \quad (1)$$

Here η_{LH} is the light harvesting efficiency (i.e. the fraction of incident photons absorbed), η_{inj} is the electron-injection efficiency, I_0 is the incident photon flux, τ is the free electron lifetime and d is the thickness of the TiO_2 layer (τ corresponds to the inverse of the pseudo first-order rate constant for back electron-transfer to I_3^-). The V_{OC} value is determined by the ratio of electron concentrations under illumination and in the dark,

$$V_{\text{OC}} = \frac{k_{\text{B}} T}{q} \ln \frac{n_{\text{light}}}{n_{\text{dark}}} \quad (2a)$$

where n_{dark} is determined by the difference between the conduction band edge energy E_{c} and the redox Fermi level energy E_{Fn} .

$$n_{\text{dark}} = N_{\text{c}} e^{-\left(\frac{E_{\text{c}} - E_{\text{Fn}}}{k_{\text{B}} T}\right)} \quad (2b)$$

The higher V_{OC} for the cell sensitized with [6]PF₆ could be due to several different factors. Since η_{LH} and τ are expected to remain essentially constant for all four dyes, the most probable difference between them is either η_{inj} or the difference between E_{c} and E_{Fn} .

The second important characteristic of a DSSC is the short-circuit current density, J_{SC} . For AM 1.5 illumination, J_{SC} is determined by the product of the

efficiencies for light harvesting, electron injection and electron collection (η_{col}). In principle all three efficiencies may depend on photon energy, so that J_{SC} corresponds to the integral

$$J_{\text{SC}} = q \int \eta_{\text{LH}}(\lambda) \eta_{\text{inj}}(\lambda) \eta_{\text{col}}(\lambda) I(\lambda) d\lambda \quad (3)$$

where q is the elementary charge. J_{SC} follow the sequence $[\mathbf{8}]\text{PF}_6 > [\mathbf{6}]\text{PF}_6 \gg [\mathbf{7}]\text{PF}_6 = [\mathbf{5}]\text{PF}_6$ (Table 4, Figure 12). The J_{SC} values are at least an order of magnitude lower than those measured for identical cells sensitized with the standard ruthenium complex N719 ($J_{\text{SC}} = 11.4 \text{ mA cm}^{-2}$), so clearly electron losses are much higher with the new stilbazolium dyes. The electrolytes used here give η_{col} close to 100% with N719[21], so it can be assumed that this factor is not the origin of the differences in J_{SC} in the present studies. All of the dyes $[\mathbf{5}\text{--}\mathbf{8}]\text{PF}_6$ absorb very strongly in the visible region, with ε values substantially higher than those of N719 and similar species (ca. $1.5\text{--}2 \times 10^4 \text{ M}^{-1} \text{ cm}^{-1}$). The red shifts of the ICT bands of the Me-substituted dyes with respect to their Ph analogues (Figure 2) could lead to slightly higher η_{LH} values, so this factor cannot explain the higher J_{SC} values for the latter. This leaves differences in η_{inj} as the most likely explanation.

The difference between the dyes is also evident in the IPCE plots shown in Figure 13. The highest IPCE is observed for the cell fabricated with $[\mathbf{8}]\text{PF}_6$, and the lowest for the cell sensitized with $[\mathbf{5}]\text{PF}_6$. The peak IPCE observed for $[\mathbf{8}]\text{PF}_6$ is only ca. 9%, an order of magnitude lower than that for the best Ru-based sensitizers. These low IPCE values are consistent with the low J_{SC} values recorded for the cells.

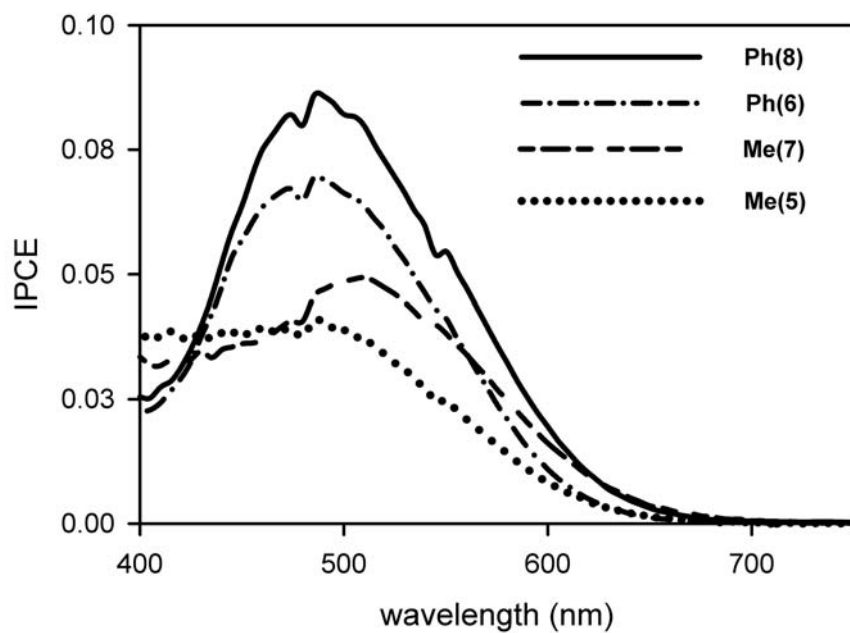


Fig. 13. IPCE plots for TiO₂-based DSSCs containing [5–8]PF₆.

In order to test whether poor injection is the cause of the low currents and voltages observed, the performance of cells sensitized with [6]PF₆ and filled with electrolytes A and B was compared. The results are shown in Figure 14.

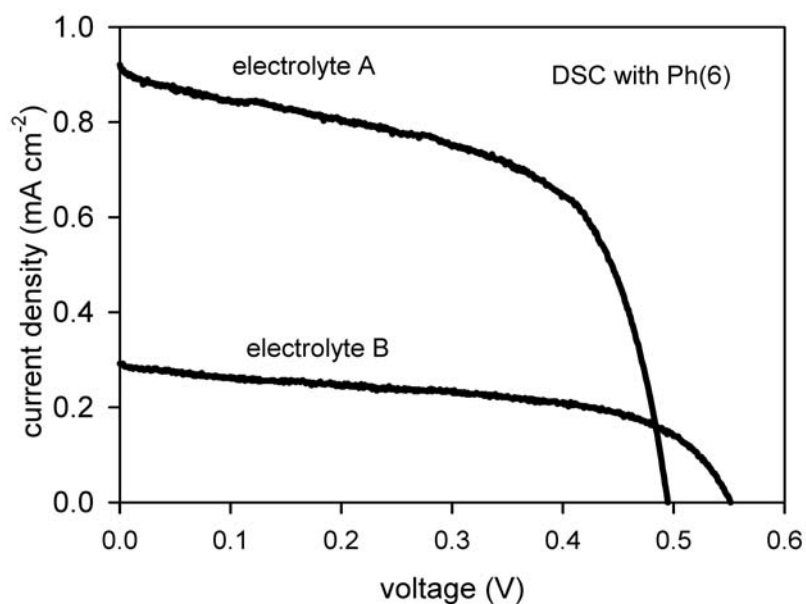


Fig. 14. AM 1.5 current voltage characteristics of TiO₂-based DSSCs containing [6]PF₆ with electrolytes A and B.

Substitution of electrolyte A (which contains Na^+) by the sodium-free electrolyte B lowers the J_{SC} values by a factor of 3, but increases V_{OC} by ca. 60 mV. The lower current and higher voltage in the sodium-free electrolyte can be attributed to destabilization of the TiO_2 conduction band relative to the I_3^-/I^- Fermi level. Alkali metal ions are known to lower the E_c of TiO_2 as a consequence of changing the surface dipole [22]. This sensitivity of the cell performance to electrolyte composition suggests that η_{inj} is influenced by the alignment of the excited state energy and E_c , but it is likely that other factors are also responsible for the low efficiencies.

Table 5

Current/voltage characteristics of ZnO-based DSSCs containing [7]PF₆, [8]PF₆ or D149.

dye	electrolyte	J_{SC} (mA cm ⁻²)	V_{OC} (mV)	FF (%)	η (%)
[7]PF ₆	1	1.680	503	48.3	0.4
[7]PF ₆	6	0.966	485	55.2	0.3
[7]PF ₆	2	2.334	524	55.9	0.7
[8]PF ₆	2	2.700	492	60.0	0.8
D149	2	8.382	668	35.0	2.0

While the data presented here do not relate to excited state properties, so provide only rough a guide, both the electrochemical measurements and the TD-DFT calculations (Table 4) indicate that the LUMO energies of the new dyes are too low with respect to the conduction band of TiO_2 to allow efficient electron injection. Experiments in acetonitrile-based electrolytes have yielded an E_c value of ca. -0.7 V vs Ag–AgCl [23], similar to or even higher than the potentials for reduction of the pyridinium groups in [5–8]PF₆. Furthermore, DFT calculations have been used to derive E_c values of ca. $-(4-5)$ eV for TiO_2 nanoparticles [24], higher than our predicted LUMO energies. Our TD-DFT calculations also indicate that the LUMOs feature very little electron density on the acid-functionalized phenyl rings (Figure 11). By contrast, the direct attachment of carboxylate groups to the electron-accepting 2,2'-bipyridyl ligands in Ru^{II}-based dyes gives a much more favourable electron

density distribution in the excited states. Time-resolved studies of electron injection could give more information on this aspect of the sensitization process.

Although TiO_2 has been used most widely, various metal oxides can be used in DSSCs [1]. Therefore, we have also carried out studies with the representative dye salts [7] PF_6 and [8] PF_6 using ZnO instead of TiO_2 -based photoanodes, noting that the number of carboxylate substituents does not greatly affect the dye performance on the latter (Table 4). When compared with the TiO_2 -based photoanodes, much shorter immersion times were used (only 30 min cf. 16 h). This change is intended to minimize chemical reactions between the dyes and ZnO, which is known to be unstable under both acidic and basic conditions [1f,25]. Five different electrolytes were tested with [7] PF_6 in order to find the most suitable. Dye desorption and thus a significant decrease of the photocurrent with time is observed for electrolytes 4 and 5. Desorption is also observed with electrolyte 6, although not as strongly as with 4 and 5. The data obtained by using electrolytes 1, 2 and 6 are shown in Table 5 and I-V curves are depicted in Figure 15. Given that electrolyte 2 clearly gives the best performance, [8] PF_6 was also tested using this mixture. The I-V curves obtained under these conditions with [7] PF_6 , [8] PF_6 or the indoline reference dye D149 [26] are shown in Figure 15.

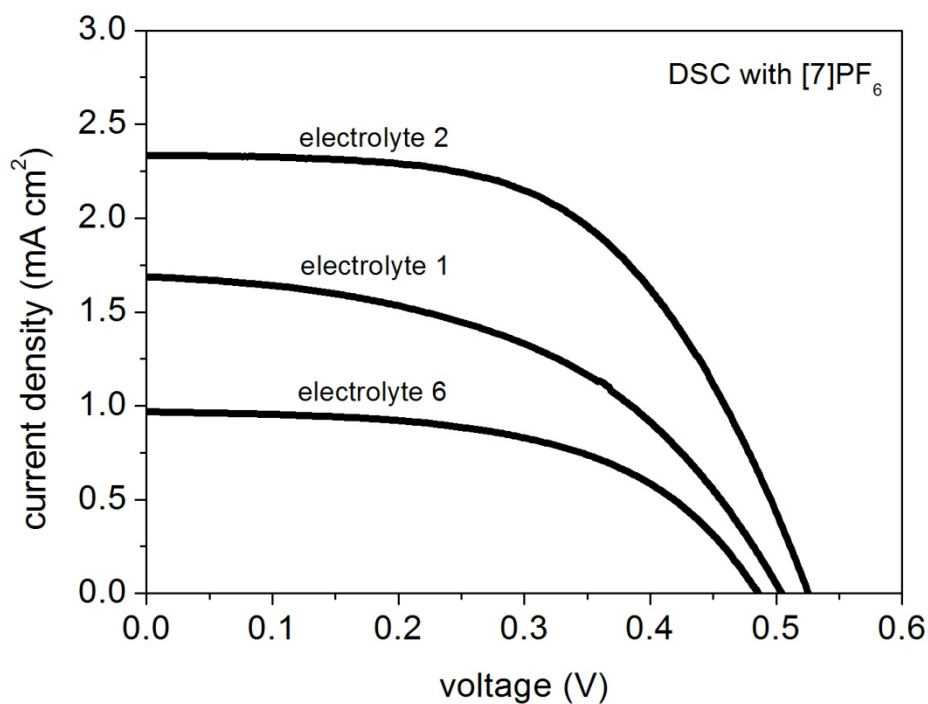


Fig. 14. AM 1.5 current voltage characteristics of ZnO-based DSSCs containing [7]PF₆ with electrolytes 1, 2 and 6.

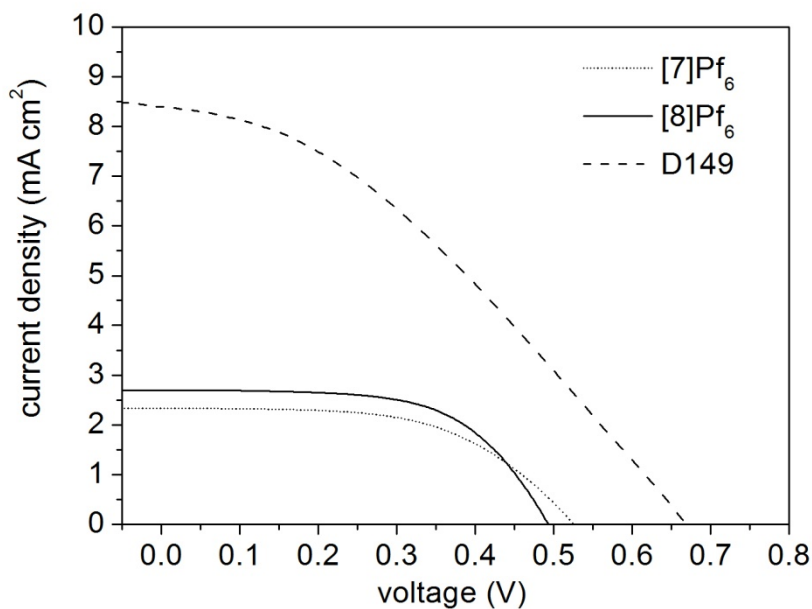


Fig. 15. AM 1.5 current voltage characteristics of ZnO-based DSSCs containing [7]PF₆, [8]PF₆ or D149 with electrolyte 2.

Comparison with the data obtained using TiO₂-based photoanodes (Table 4) shows that the overall efficiencies of solar cells sensitized with [7]PF₆ or [8]PF₆ are improved 3–4-fold by switching to ZnO. Since the E_c value of ZnO is more negative by ca. 100 mV when compared with that of TiO₂ (anatase) [27], this factor can not be the cause of the increased performance of the new dyes with ZnO. It may be that the relatively higher electron mobility of ZnO which facilitates electron transport is important. While the studies using both metal oxides show that the Ph-substituted dyes are more efficient than their Me analogues, the difference between [7]PF₆ and [8]PF₆ is less pronounced with ZnO.

The performance of the new dyes is still substantially below that of a common benchmark (in this case D149, Table 5), with J_{SC} values about 30% as large and V_{OC} values 143–176 mV lower. Nevertheless, these results are encouraging in the context of a first investigation with a new class of dye. In order to improve the performance of stilbazolium dyes, further tuning of both the energy levels and the electron donor-acceptor coupling will be necessary. One possibility that may be expected to affect both aspects beneficially is to use *N*-(2-carboxyvinyl)- instead of *N*-arylpyridinium groups.

4. Conclusions

BJC TO WRITE

Acknowledgements

We thank the EPSRC for support in the form of a PhD studentship (YTT) and also DyStar UK Ltd and the University of Manchester for funding a PhD studentship (OAB). We are grateful to Dr Joseph J. W. McDouall (Manchester) for advice concerning TD-DFT calculations. EG and JAA thank the Ministerio de Ciencia e Innovación of Spain for project HOPE CSD2007-00007 (Consolider-Ingenio 2010), CTQ2009-10477 (TRANSLIGHT), and a FPU studentship, and Junta de Andalucía (Andalusian Regional Government) under projects P07-FQM-02595, P07-FQM-02600, and P09-FQM-04938.

+ADDITIONS REGARDING BATH DSSC STUDIES?

The work in Bath was supported by EPSRC (EP/E035469/1).

References

- [1] (a) Nazeeruddin MdK, Grätzel M. Conversion and storage of solar energy using dye-sensitized nanocrystalline TiO₂ cells. In *Comprehensive Coordination Chemistry II*, Vol. 9. McCleverty JA, Meyer TJ, Eds., Pergamon Press, Oxford, UK, 2004, pp. 719–758; (b) Robertson N, Optimizing dyes for dye-sensitized solar cells. *Angew Chem Int Ed* 2006; 45: 2338–45; (c) Durrant JR, Haque SA, Palomares E. Photochemical energy conversion: from molecular dyads to solar cells. *Chem Commun* 2006; 3279–89; (d) Peter LM. Characterization and modeling of dye-sensitized solar cells. *J Phys Chem C* 2007; 111: 6601–12; (e) Special issue on organic photovoltaics. *Acc Chem Res* 2009; 42: 1689–1857; (f) Hagfeldt A; Boschloo G; Sun L-C; Kloo L; Pettersson H. Dye-sensitized solar cells. *Chem Rev* 2010; 110: 6595–663.
- [2] O'Regan B, Grätzel M. A low-cost, high-efficiency solar cell based on dye-sensitized colloidal TiO₂ films. *Nature* 1991; 353: 737–40.
- [3] (a) Ning Z-J, Tian H. Triarylamine: a promising core unit for efficient photovoltaic materials. *Chem Commun* 2009; 5483–95; (b) Mishra A, Fischer MKR, Bäuerle P. Metal-free organic dyes for dye-sensitized solar cells: from structure:property relationships to design rules. *Angew Chem Int Ed* 2009; 48: 2474–99; (c) Pastore M, Mosconi E, De Angelis F, Grätzel M. A computational investigation of organic dyes for dye-sensitized solar cells: benchmark, strategies, and open issues. *J Phys Chem C* 2010; 114: 7205–12.
- [4] Selected examples: (a) Zhang G-L, Bala H, Cheng Y-M, Shi D, Lv X-J, Yu Q-J, et al. High efficiency and stable dye-sensitized solar cells with an organic chromophore featuring a binary π -conjugated spacer. *Chem Commun* 2009, 2198–200; (b) Li Q-Q, Lu L-L, Zhong C, Huang J, Huang Q, Shi J, et al. New pyrrole-based organic dyes for dye-sensitized solar cells: convenient syntheses and high efficiency. *Chem Eur J* 2009; 15: 9664–68; (c) Choi H, Kang SO, Ko J, Gao G, Kang HS, Kang M-S, et al. An efficient dye-sensitized solar cell

- with an organic sensitizer encapsulated in a cyclodextrin cavity. *Angew Chem Int Ed* 2009, 48, 5938–41; (d) Im H, Kim S, Park C, Jang S-H, Kim C-J, Kim K, et al. High performance organic photosensitizers for dye-sensitized solar cells. *Chem Commun* 2010; 46: 1335–37; (e) Choi H, Raabe I, Kim D, Teocoli F, Kim C, Song K, et al. High molar extinction coefficient organic sensitizers for efficient dye-sensitized solar cells. *Chem Eur J* 2010; 16: 1193–201; (f) Chen C-H, Hsu Y-C, Chou H-H, Thomas KRJ, Lin JT, Hsu CP. Dipolar compounds containing fluorene and a heteroaromatic ring as the conjugating bridge for high-performance dye-sensitized solar cells. *Chem Eur J* 2010; 16: 3184–93; (g) Liu X-Z, Zhang W, Uchida S, Cai L-P, Liu B, Ramakrishna S. An efficient organic-dye-sensitized solar cell with in situ polymerized poly(3,4-ethylenedioxythiophene) as a hole-transporting material. *Adv Mater* 2010; 22: E150–E155.
- [5] (a) Coe BJ, Harris JA, Asselberghs I, Clays K, Olbrechts G, Persoons A, et al. Quadratic nonlinear optical properties of *N*-aryl stilbazolium dyes. *Adv Funct Mater* 2002; 12: 110–6; (b) Coe BJ, Harris JA, Asselberghs I, Wostyn K, Clays K, Persoons A, et al. Quadratic optical nonlinearities of *N*-methyl and *N*-aryl pyridinium salts. *Adv Funct Mater* 2003; 13: 347–57; (c) Coe BJ, Foxon SP, Harper EC, Harris JA, Helliwell M, Raftery J, et al. The syntheses, structures and nonlinear optical and related properties of salts with julolidinyl electron donor groups. *Dyes Pigments* 2009; 82: 171–86.
- [6] Other recent examples: (a) Coe BJ. Switchable nonlinear optical metallochromophores with pyridinium electron acceptor groups. *Acc Chem Res* 2006; 39: 383–93; (b) Kim HS, Sohn KW, Jeon Y, Min H, Kim D, Yoon KB. Aligned inclusion of *n*-propionic acid tethering hemicyanine into silica zeolite film for second harmonic generation. *Adv Mater* 2007; 19: 260–3; (c) Figi H, Mutter L, Hunziker C, Jazbinšek M, Günter P, Coe BJ. Extremely large nonresonant second-order nonlinear optical response in crystals of the stilbazolium salt DAPSH. *J Opt Soc Am B* 2008; 25: 1786–93; (d) Compain J-

- D, Mialane P, Dolbecq A, Marrot J, Proust A, Nakatani K, et al. Second-order nonlinear optical properties of polyoxometalate salts of a chiral stilbazolium derivative. *Inorg Chem* 2009; 48: 6222–28; (e) Coe BJ, Fielden J, Foxon SP, Brunshwig BS, Asselberghs I, Clays K, et al. Combining very large quadratic and cubic nonlinear optical responses in extended, tris-chelate metallochromophores with six π -conjugated pyridinium substituents. *J Am Chem Soc* 2010; 132, 3496–513.
- [7] Selected examples: (a) Kim Y-H, Das A, Zhang H-Y, Dutta PK. Zeolite membrane-based artificial photosynthetic assembly for long-lived charge separation. *J Phys Chem. B* 2005; 109: 6929–32; (b) Lainé PP, Bedioui F, Loiseau F, Chiorboli C, Campagna S. Conformationally gated photoinduced processes within photosensitizer–acceptor dyads based on osmium(II) complexes with triarylpyridinio-functionalized terpyridyl ligands: insights from experimental study. *J Am Chem Soc* 2006; 128: 7510–21; (c) Weber JM, Rawls MT, MacKenzie VJ, Limoges BR, Elliott CM. High energy and quantum efficiency in photoinduced charge separation. *J Am Chem Soc* 2007; 129: 313–20; (d) Zhang H-Y, Rajesh CS, Dutta PK. Ruthenium polypyridyl complexes containing a conjugated Ligand L_{DQ} ($L_{DQ} = 1$ -[4-(4'-methyl)-2,2'-bipyridyl]-2-[4-(4'-*N,N'*-tetramethylene-2,2'-bipyridinum)]ethene): synthesis, characterization, and photoinduced electron transfer at solution-zeolite interfaces. *J Phys Chem C* 2009; 113: 4623–33.
- [8] SAINT (Version 6.45) and SADABS (Version 2.10), Bruker AXS Inc, Madison: Wisconsin, USA, 2003.
- [9] Sheldrick GM. Phase Annealing in *SHELX-90*: Direct Methods for Larger Structures. *Acta Crystallogr Sect A* 1990; 46: 467–73.
- [10] Sheldrick GM. *SHELXL 97*, Program for crystal structure refinement; University of Göttingen: Göttingen, Germany, 1997.
- [11] *SHELXTL* (Version 6.10), Bruker AXS Inc, Madison: Wisconsin, USA, 2000.

- [12] Becke AD. Density-functional thermochemistry. III. The role of exact exchange. *J Chem Phys* 1993; 98: 5648–52.
- [13] Krishnan R; Binkley JS; Seeger R; Pople JA. Self-consistent molecular orbital methods. XX. A basis set for correlated wave functions. *J Chem Phys* 1980; 72: 650–4.
- [14] Gaussian 03, Revision C.02, Frisch MJ; Trucks GW; Schlegel HB; Scuseria GE; Robb MA; Cheeseman VG; Montgomery JA, Vreven Jr. T; Kudin KN; Burant JC; Millam JM; Iyengar SS; Tomasi J; Barone V; Mennucci B; Cossi M; Scalmani G; Rega N; Petersson GA; Nakatsuji H; Hada M; Ehara M; Toyota K; Fukuda R; Hasegawa J; Ishida M; Nakajima T; Honda Y; Kitao O; Nakai H; Klene M; Li X; Knox JE; Hratchian HP; Cross JB; Adamo C; Jaramillo J; Gomperts R; Stratmann RE; Yazyev O; Austin AJ; Cammi R; Pomelli C; Ochterski JW; Ayala PY; Morokuma K; Voth GA; Salvador P; Dannenberg JJ; Zakrzewski VG; Dapprich S; Daniels AD; Strain MC; Farkas O; Malick DK; Rabuck AD; Raghavachari K; Foresman JB; Ortiz JV; Cui Q; Baboul AG; Clifford S; Cioslowski J; Stefanov BB; Liu G; Liashenko A; Piskorz P; Komaromi I; Martin RL; Fox DJ; Keith T; Al-Laham MA; Peng CY; Nanayakkara A; Challacombe M; Gill PMW; Johnson B; Chen W; Wong MW; Gonzalez C; Pople JA; Gaussian, Inc., Wallingford CT, 2004.
- [15] (a) Barone V; Cossi M. Quantum calculation of molecular energies and energy gradients in solution by a conductor solvent model. *J Phys Chem A* 1998; 102: 1995–2001; (b) Cossi M; Rega N; Scalmani G; Barone V. Energies, structures, and electronic properties of molecules in solution with the C-PCM solvation model. *J Comp Chem* 2003; 24: 669–81.
- [16] O’Boyle NM, Tenderholt AL, Langner KM. cclib: A library for package-independent computational chemistry algorithms. *J Comp Chem* 2008; 29: 839–45.

- [17] Kwon O; Barlow S; Odom SA; Beverina L; Thompson NJ; Zojer E; Brédas J-L; Marder SR. Aromatic amines: a comparison of electron-donor strengths. *J Phys Chem A* 2005; 109: 9346–52.
- [18] Liu Y-L; Feng J-K; Ren A-M. Theoretical study of optical and electronic properties of the bis-dipolar diphenylamino-encapped oligoarylfluorenes as promising light emitting materials. *J Phys Org Chem* 2007; 20: 600–9.
- [19] Peter LM. Dye-sensitized nanocrystalline solar cells. *Phys Chem Chem Phys* 2007; 9: 2630–42.
- [20] Dye sensitized solar cells. Kalyanasundranam K, Ed. EPFL Press, Lausanne, Switzerland, 2010.
- [21] Wang HX; Peter LM. A comparison of different methods to determine the electron diffusion length in dye-sensitized solar cells. *J Phys Chem C* 2009; 113: 18125–33.
- [22] Park N-G; Chang S-H; van de Lagemaat J; Kim K-J; Frank AJ. Effect of cations on the open-circuit photovoltage and the charge-injection efficiency of dye-sensitized nanocrystalline rutile TiO₂ films. *Bull Korean Chem Soc* 2000; 21: 985–8.
- [23] Lemon BI; Liu F; Hupp JT. Electrochemical, spectral, and quartz crystal microgravimetric assessment of conduction band edge energies for nanocrystalline zirconium dioxide/solution interfaces. *Coord Chem Rev* 2004; 248: 1225–30.
- [24] (a) Kusama H; Orita H; Sugihara H. DFT investigation of the TiO₂ band shift by nitrogen-containing heterocycle adsorption and implications on dye-sensitized solar cell performance. *Solar Energy Materials & Solar Cells* 2008; 92: 84–7; (b) De Angelis F; Fantacci S; Selloni A. Alignment of the dye's molecular levels with the TiO₂ band edges in dye-sensitized solar cells: a DFT–TDDFT study. *Nanotechnology* 2008; 19: 424002.

- [25] Keis K; Lindgren J; Lindquist S-E; Hagfeldt A. Studies of the adsorption process of Ru complexes in nanoporous ZnO electrodes. *Langmuir* 2000; 16: 4688–94.
- [26] (a) Onwona-Agyeman B.; Kaneko S.; Kumara A.; Okuya M.; Murakami K.; Konno A.; Tennakone K. Sensitization of nanocrystalline SnO₂ films with indoline dyes. *Jpn J Appl Phys, Part 2* 2005; 44: L731–33; (b) Minoura H.; Yoshida T. Electrodeposition of ZnO/dye hybrid thin films for dye-sensitized solar cells. *Electrochem* 2008; 76: 109–17; (c) Guillén E; Idígoras J; Berger T; Anta JA; Fernández-Lorenzo C.; Alcántara R.; Navas J.; Martín-Calleja J. ZnO-based dye solar cell with pure ionic-liquid electrolyte and organic sensitizer: the relevance of the dye-oxide interaction in an ionic-liquid medium. *Phys Chem Chem Phys* 2011; 13: 207–13.
- [27] (a) Nozik, A. Photochemistry: Applications to solar energy conversion, *Annu Rev Phys Chem* 1978; 29: 189–222; (b) Photocatalysis: Fundamentals and Applications. Serpone N, Pelizzetti E, Eds., Wiley, New York, 1989.